Between Imide, Imidyl and Nitrene – An Imido Iron Complex in Two Oxidation States

Sascha Reith,[a] Serhiy Demeshko,[b] Beatrice Battistella,[c] Alexander Reckziegel,[a] Christian Schneider,[a] Andreas Stoy,[a] Crispin Lichtenberg,[a] Franc Meyer,[b] Dominik Munz*,[d,e] C. Gunnar Werncke*,[a]

a) Philipps-University Marburg, Department of Chemistry, Hans-Meerwein-Straße 4, D-35037 Marburg, Germany

b) University of Göttingen, Institute for Inorganic Chemistry, Tammannstraße 4, D-37077 Göttingen, Germany

c) Humboldt-University Berlin, Institute for Chemistry, Brook-Taylor-Straße 2, D-12489 Berlin, Germany

d) Saarland University, Inorganic Chemistry: Coordination Chemistry, Campus C4.1, D-66123 Saarbrücken, Germany

e) Friedrich-Alexander University Erlangen-Nürnberg, Inorganic Chemistry, Egerlandstraße 1, D-91058 Erlangen, Germany

Table of Contents

General considerations

All manipulations were carried out in a glovebox or using Schlenk-type techniques under a dry argon atmosphere. Used solvents were dried by continuous distillation over sodium metal for several days, degassed via three freeze-pump cycles and stored over molecular sieves 4 Å. The ^{1}H NMR spectra were recorded on a *Bruker AV III 500* or a *Bruker AV II 300* NMR spectrometers. Chemical shifts are reported in ppm relative to the residual proton signals of the solvent (for ^{1}H) or relative to the signal of the solvent itself (^{13}C). The ^{31}P NMR spectra were recorded on a *Bruker AV III HD 300* and chemical shifts are reported in ppm relative to H_3PO_4. $w_{1/2}$ is the line width of a signal at half its maximum intensity. Integrals of the broad signals of the silylamide units were obtained directly ore by peak fitting (in case of overlapping signals) using the MestReNova software package. IR measurements were conducted on a *Bruker Alpha ATR-IR* spectrometer. Elemental analyses were performed by the "in-house" service of the Chemistry Department of the Philipps University Marburg, Germany using a CHN(S) analyzer *vario MICRO Cube* (*Elementar)*. The UV/VIS measurement were recorded on an *Analytik Jena Specord S600* spectrometer using *WinASPECT* software and an *UNISOKU CoolSpeK Cryostat*. The distinct signal at around 680 nm is assigned to a lamp change. Solution magnetic susceptibilities were determined by the Evans method.[1] EPR measurements considering the conversion of TEMPO–H to the TEMPO radical were carried out at room temperature at X-band (9.38 GHz) by using a *Bruker/Magnettech ESR 5000* spectrometer (experimental parameters: microwave frequency = 9.38 GHz, microwave power = 1 mW, modulation amplitude = 0.5 G and 2 G, modulation frequency = 100 kHz). 2.2.2-cryptand (crypt.222), 1,4-cyclohexadiene, 2,2,6,6-tetramethylpiperidinyloxyl, carbon disulfide (CS_2), and tetramethylsilane (TMS) were obtained commercially (Sigma-Aldrich, Acros, Strem, Alfa Aesar) and -if not noted otherwise- used as received. 1,4-cyclohexadiene and carbon disulfide were degassed, transferred into a glovebox and stored at −35 °C. [Fe(N{Dipp}SiMe$_3$)$_2$],[2] and 1-azido-2,4,6-trimethylbenzene (N_3Mes)[3] and 1-hydroxy-2,2,6,6-tetramethylpiperidin (TEMPO-H)[4] were prepared according to the respective literature procedures.

Synthesis of K{crypt.222}[Fe(N{Dipp}SiMe$_3$)]

580 mg (1.05 mmol, 1 equiv.) [Fe(N{Dipp}SiMe$_3$)$_2$] were dissolved in 20 mL Et_2O. Addition of 180 mg (1.31 mmol, 1.25 equiv.) KC_8 at –30 °C resulted in a color change from red to brown. After stirring the mixture for 10 minutes the suspension was filtered and the filtrate was layered with a solution of 414 mg (1.10 mmol, 1.05 equiv.) crypt.222 in 15 mL Et_2O. Storage at −35°C led to the precipitation of a dark green crystalline solid. After filtration all remaining volatiles were removed *in vacuo* to afford 909 mg (0.93 mmol, 89%) of K{crypt.222}[Fe(N{Dipp}SiMe$_3$)$_2$].

^{1}H-NMR (THF-d_8, 298 K, ppm, 500 MHz): 28.71 (s, $w_{1/2}$ = 367 Hz), 27.35 (s, $w_{1/2}$ = 462.4 Hz), 12.17 (s, $w_{1/2}$ = 166 Hz), 2.76 (s, $w_{1/2}$ = 37 Hz, crypt), 2.70 (s, $w_{1/2}$ = 41 Hz, crypt), 1.84 (s, $w_{1/2}$ = 35 Hz, crypt), 1.22 (s, $w_{1/2}$ = 9.5 Hz), −0.6 (s, $w_{1/2}$ = 950 Hz,), −100.5 (s, $w_{1/2}$ = 1420 Hz).

IR (ATR, cm^{-1}) ν: 2942 (m), 2884 (m), 2838 (m), 1577 (w), 1469 (w), 1453 (w), 1448 (w),1423 (m), 1356 (m), 1314 (m), 1294 (w), 1234 (s), 1223 (s), 1193 (m), 1135 (m), 1100 (vs), 1072 (s), 1051 (w), 947 (m), 926 (vs), 880 (w), 836 (vs), 780 (s), 747 (m), 660 (m), 617 (w), 538 (w), 521 (w), 429 (m).

Elemental analysis: calcd. (%) for $C_{48}H_{88}FeKN_4O_6Si_2$ (968.37 g mol^{-1}): C 59.54 H 9.16 N 5.79; found: C 59.74 H 9.112 N 5.83.

Solution magnetic susceptibility: μ_{eff} = 4.66 μ_B (THF-d_8+ 1% $Si(CH_3)_4$, 500 MHz, 298 K).

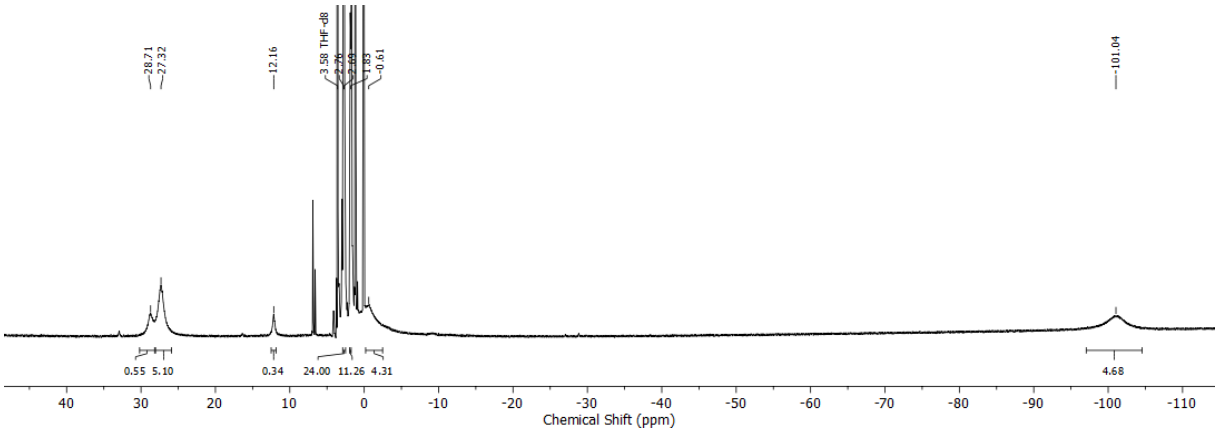

Figure S1. ^{1}H-NMR spectrum of K{crypt.222}[Fe(N{Dipp}SiMe$_3$)$_2$] in THF-d_8 (298 K, 300 MHz).

Synthesis of K{crypt.222}[Fe(NMes)(N{Dipp}SiMe$_3$)$_2$] (K{crypt.222}[1])

Path A:
80 mg (0.1 mmol, 1 equiv.) K{crypt}[Fe(N{Dipp}SiMe$_3$)$_2$] were dissolved in a mixture of 2 mL Et_2O and 1 mL THF. Addition of 14 mg (0.1 mmol, 1 equiv.) N_3Mes at −35 °C resulted in an immediate color change from green to dark green under concomitant gas evolution. After stirring the mixture for 5 minutes, the mixture was layered with 3 mL *n*-pentane and stored at −35 °C. After one day, the solution was removed via pipette and the remaining dark green crystals were rinsed with 2x3 mL pentane. Drying *in vacuo* yielded 78 mg (0.1 mmol, 86%) K{crypt.222}[**1**].

Path B:
100 mg (0.15 mmol, 1 equiv.) [Fe(NMes)(N{Dipp}SiMe$_3$)$_2$] ([**1**]) were dissolved in 3 mL Et_2O. After addition of 49.0 mg (0.14 mmol, 0.95 equiv.) crypt.222 and 22.0 mg (0.16 mmol, 1.1 equiv.) KC_8 the suspension was stirred for 30 min. Meanwhile, a color change from brown to yellowish brown was observed. The suspension was filtered, the filtrate layered with 3 mL *n*-pentane and stored at −35 °C. After one day, the solution was removed via pipette and the remaining dark yellow crystals were rinsed with 2x3 mL pentane. The crystals were characterized through X-ray diffraction analysis and ^{1}H NMR spectroscopy.

^{1}H-NMR (THF-d_8, 298 K, ppm, 300 MHz): 45.2 (s, $w_{1/2}$ = 85 Hz), 11.0 (s, $w_{1/2}$ = 1060 Hz), 5.83 (s, $w_{1/2}$ = 870 Hz), 3.50 (s, $w_{1/2}$ = 21.2 Hz), 2.50 (s, $w_{1/2}$ = 14.7 Hz), −3.20 (s, $w_{1/2}$ = 475 Hz), −39.6 (s, $w_{1/2}$ = 470 Hz).

IR (ATR, cm^{-1}) ν: 2975 (m), 2880 (m), 2973 (m), 1596 (w), 1465 (w), 1425 (s), 1350 (s, 1298 (s), 1240 (vs), 1194 (s), 1090 (vs), 1073 (vs), 946 (s), 900 (s), 825 (vs), 773 (s), 738 (m), 669 (m), 542 (w), 432 (w).

Elemental analysis: calcd. (%) for $C_{57}H_{99}FeKN_5O_6Si_2$ (1101.56 g mol^{-1}): C 62.15 H 9.06 N 6.36; found: C 61.82 H 8.851 N 6.38.

Solution magnetic susceptibility: μ_{eff} = 5.39 μ_B (THF-d_8+ 1% Si(CH$_3$)$_4$, 500 MHz, 298 K).

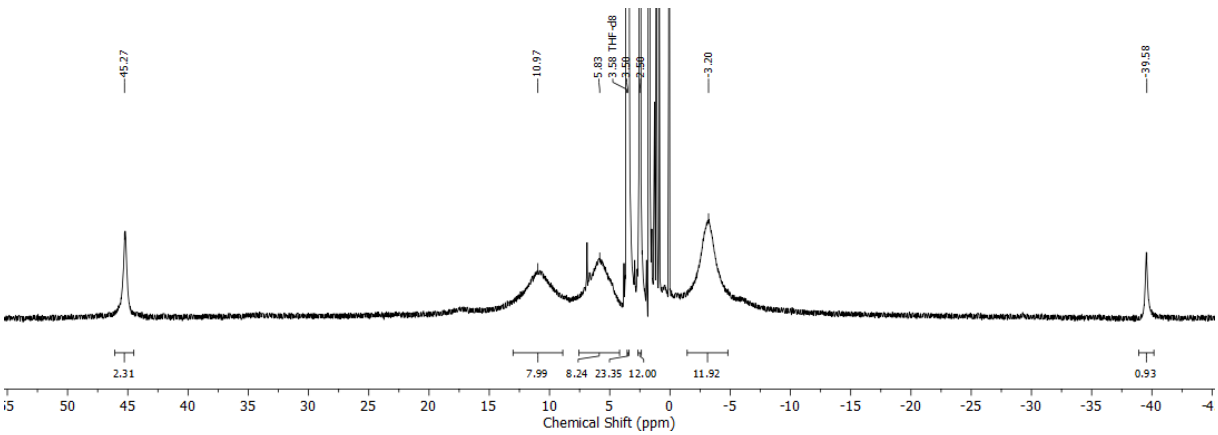

Figure S2. ^{1}H NMR spectrum of K{crypt.222}[Fe(NMes)(N{Dipp}SiMe$_3$)$_2$] (K{crypt.222}[**1**]) in THF-d_8 (298 K, 300 MHz).

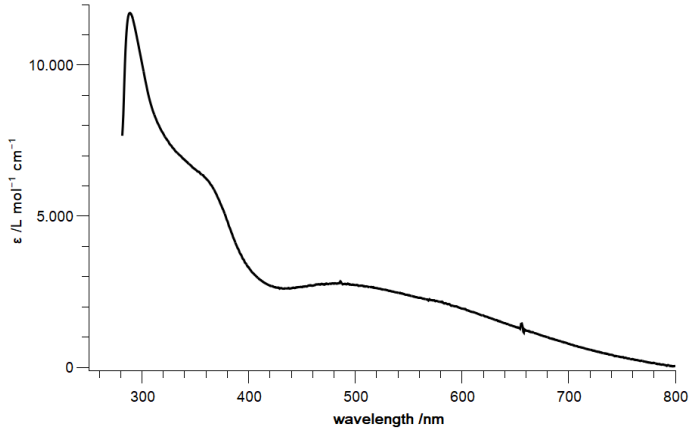

Figure S3. UV-VIS spectrum of K{crypt.222}[Fe(NMes)(N{Dipp}$SiMe_3)_2$] (K{crypt.222}[**1**]) in 1,2-DFB.

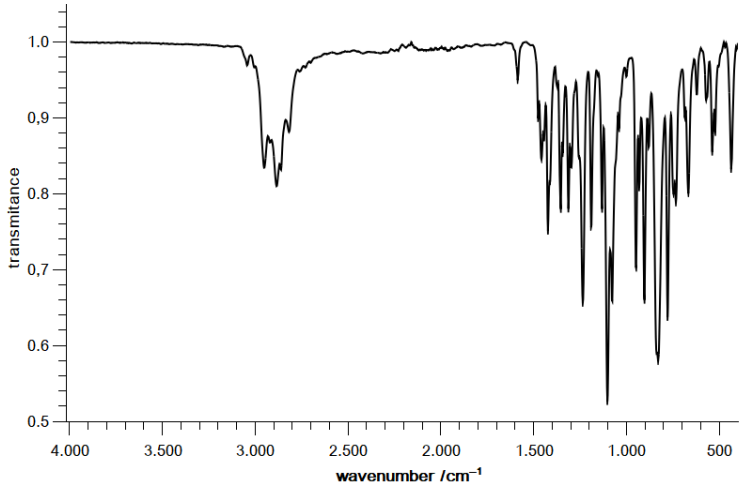

Figure S4. ATR IR-spectrum of K{crypt.222}[Fe(NMes)(N{Dipp}$SiMe_3)_2$] (K{crypt.222}[**1**]).

Synthesis of [Fe(NMes)(N{Dipp}$SiMe_3)_2$] ([1])

Path A:

50.0 mg (0.05 mmol, 1 equiv.) K{crypt.222}[**1**] were dissolved in 1 mL 1,2-difluorobenzene. After addition of 12.0 mg (0.05 mmol, 1 equiv.) AgOTf the solution was stirred for 3 hours. The solvent was removed *in vacuo* and the brown residue was dissolved in C_6D_6. The obtained ^{1}H-NMR spectra showed the formation of [**1**]. No further purification was carried out due to the high purity of [**1**] by **Path B**.

Path B:

300 mg (0.50 mmol, 1 equiv.) [Fe(N{Dipp}$SiMe_3)_2$] were dissolved in 3 mL *n*-pentane. Addition of 88 mg (0.50 mmol, 1 equiv.) N_3Mes at −35 °C resulted in an immediate color change from red to brown under concomitant gas evolution. After stirring the mixture for 30 minutes, the solution was stored at −35 °C. After two days, the solution was removed via a Pasteur pipette and the remaining brown crystals were dried *in vacuo* yielding 236 mg (0.34 mmol, 64%) [**1**].

^{1}H-NMR (C_6D_6, 298 K, ppm, 300 MHz): 78.1 (s, $w_{1/2}$ = 141 Hz), 6.82 (s), 6.72 (s), 6.62 (s), 6.55 (s, $w_{1/2}$ = 4.7 Hz), −12.3 (s, $w_{1/2}$ = 670 Hz), −41.7 (s, $w_{1/2}$ = 190 Hz).

IR (ATR, cm^{-1}) v: 3041 (m), 2951 (m), 2883 (m), 2861 (m), 2816 (m), 1606 (w), 1585 (w), 1476 (m), 1445 (m), 1422 (m), 1313 (m), 1296 (m), 1235 (s), 1132 (m), 1102 (vs), 1077 (s), 1040 (w), 948 (s), 930 (m), 905 (s), 828 (vs), 778 (s), 745 (m), 667 (w), 620 (w), 570 (m), 537 (m), 523 (m), 435 (m).

Elemental analysis: calcd. (%) for $C_{39}H_{63}FeN_2Si_2$ (685.97 g mol^{-1}): C 68.29 H 9.26 N 6.13; found: C 68.70 H 9.142 N 6.20.

Solution magnetic susceptibility: μ_{eff} = 4.98 μ_B (C_6D_6 + 1% $Si(CH_3)_4$, 500 MHz, 298 K).

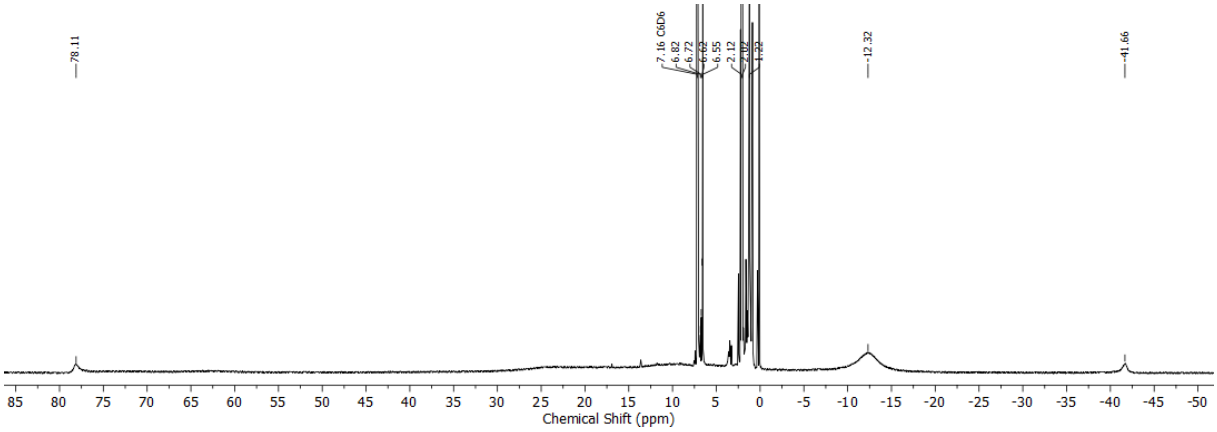

Figure S5. ^{1}H NMR spectrum of [Fe(NMes)(N{Dipp}$SiMe_3)_2$] ([**1**]) in C_6D_6 (298 K, 300 MHz).

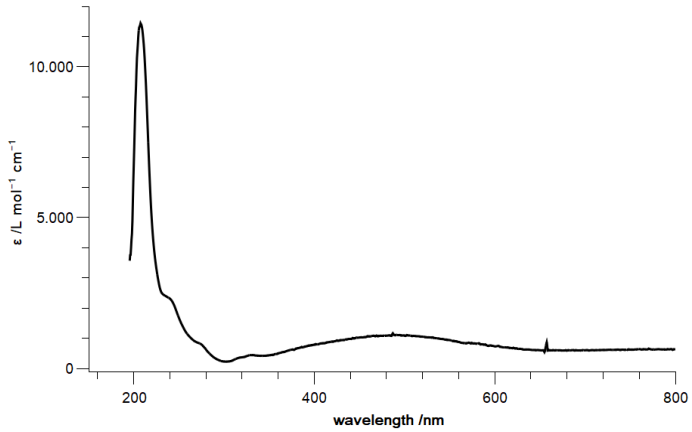

Figure S6. UV-VIS spectrum of [Fe(NMes)(N{Dipp}$SiMe_3)_2$] ([**1**]) in *n*-pentane.

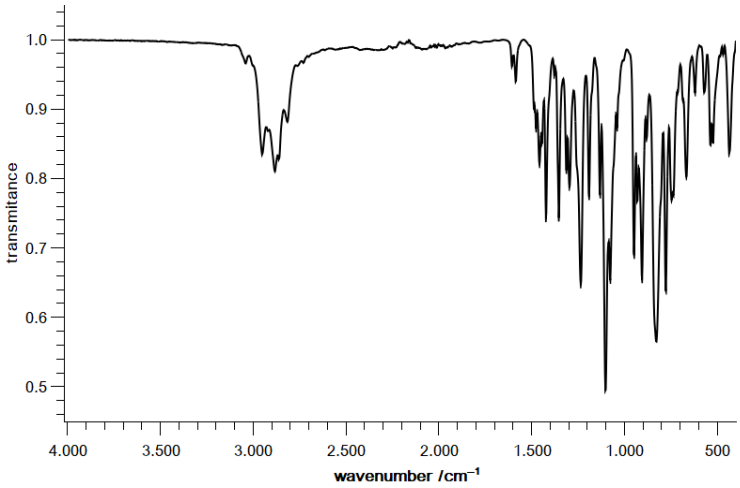

Figure S7. ATR IR-spectrum of [Fe(NMes)(N{Dipp}$SiMe_3$)$_2$] ([**1**]).

Synthesis of K{crypt.222}[Fe(N{Dipp}$SiMe_3$)$_2$(η^2-S_2CNMes)] (K{crypt.222}[2])

40 mg (0.040 mmol, 1 equiv.) K{crypt.222}[Fe(N(Dipp)$SiMe_3$)$_2$(NMes)] (K{crypt.222}[**1**]) were dissolved in 3 mL 1,2-difluorobenzene. To the solution 3 mg (0.04 mmol, 1 equiv.) CS_2 were added. While stirring the mixture for 30 minutes, a color change from dark green to reddish was observed. The solution was layered with 3 mL *n*-pentane and stored at –35 °C. After one day, the solution was removed via a Pasteur pipette and the remaining dark red crystals were rinsed with 2x3mL pentane. Drying *in vacuo* yielded 37 mg (0.03 mmol, 80%) K{crypt.222}[**2**].

^{1}H-NMR (THF-d_8, 298 K, ppm, 300 MHz): 81.3 (s, $w_{1/2}$ = 350 Hz), 15.8 (s, $w_{1/2}$ = 218 Hz), 9.64 (s, $w_{1/2}$ = 720 Hz), 3.67 (s, cryptand), 2.74 (s, cryptand, $w_{1/2}$ = 49.7 Hz), –5.61 (s, $w_{1/2}$ = 2430 Hz), –69.8 (s, $w_{1/2}$ = 340 Hz).

IR (ATR, cm^{-1}) v: 2954 (m), 2882 (m), 2864 (m), 2813 (m), 1544 (m), 1475 (w), 1457 (m), 1423 (m), 1378 (m), 1353 (w), 1296 (m), 1234 (s), 1205 (m), 1177 (w), 1131 (m), 1101 (vs), 1076 (s), 949 (s), 889 (m), 866 (m), 832 (vs), 778 (vs), 751 (s), 690 (s), 671 (m), 618 (w), 572 (w), 537 (m), 524 (m), 437 (m).

Elemental analysis: calcd. (%) for $C_{58}H_{99}FeKN_5O_6S_2Si_2$ (1177.69 g mol^{-1}): C 59.15 H 8.47 N 5.95 S 5.44; found: C 59.51 H 8.431 N 5.67 S 5.65.

Solution magnetic susceptibility: μ_{eff} = 5.84 μ_B (THF-d_8+ 1% $Si(CH_3)_4$, 500 MHz, 298 K).

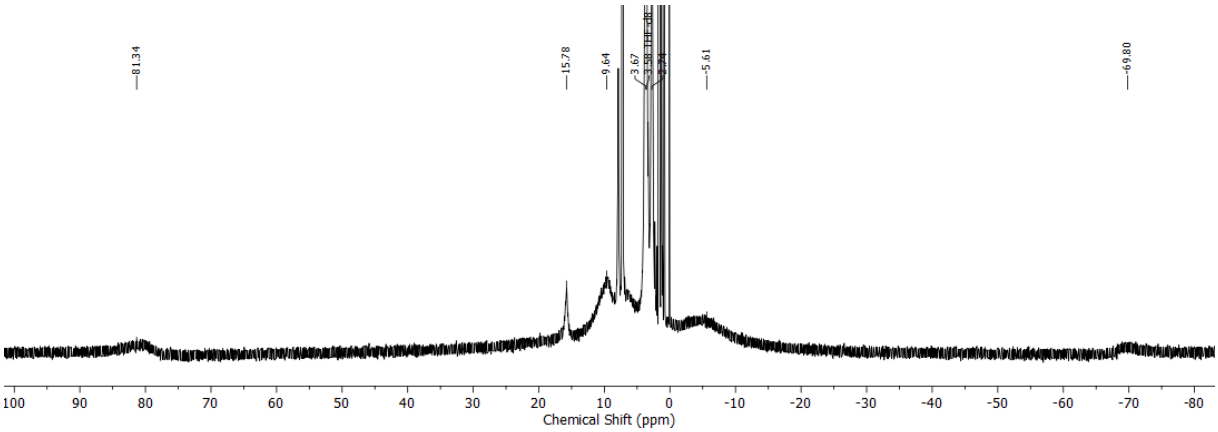

Figure S8. ^{1}H NMR spectrum of K{crypt.222}[Fe(N{Dipp}SiMe$_3$)$_2$(η^2-S$_2$CNMes)] (K{crypt.222}[**2**]) in THF-d$_8$ (298 K, 300 MHz).

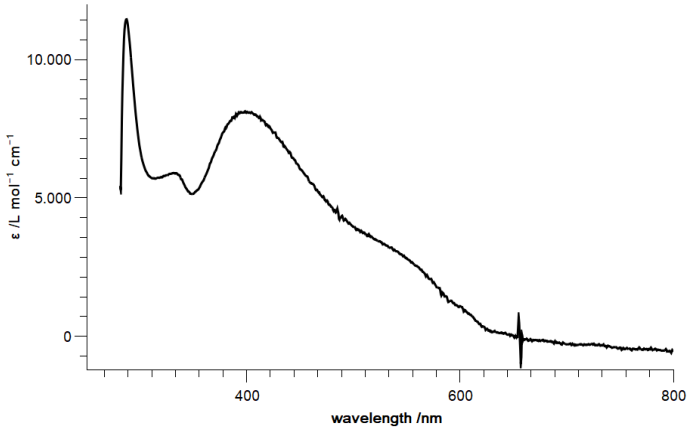

Figure S9. UV-VIS spectrum of K{crypt.222}[Fe(N{Dipp}SiMe$_3$)$_2$(η^2-S$_2$CNMes)] (K{crypt.222}[**2**]) in 1,2-DFB.

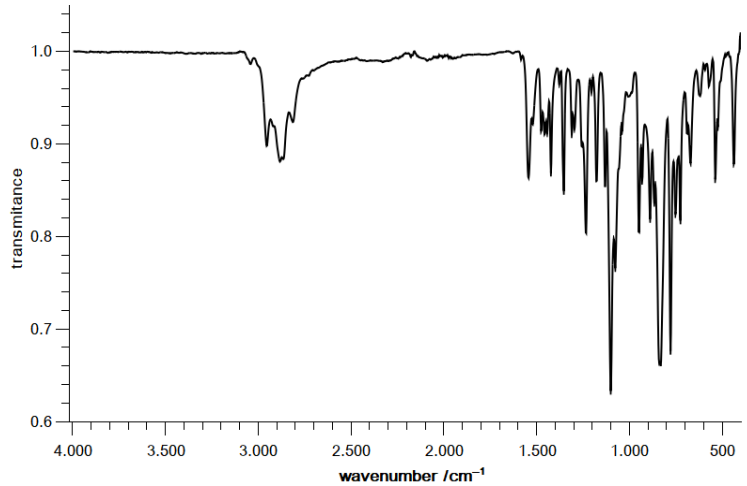

Figure S10. ATR IR-spectrum of K{crypt}[Fe(N{Dipp}SiMe$_3$)$_2$(η^2-S$_2$CNMes)] (K{crypt.222}[**2**]).

Reactivity of Imido Complexes with Phosphines

Reaction of K{crypt.222}[1] with PEt_3

To a solution of 30 mg (0.03 mmol, 1 equiv.) K{crypt.222}[**1**], dissolved in 0.4 mL THF, a second solution of 6 mg (0.05 mmol, 2 equiv.) PEt_3, dissolved in 0.2 mL THF, was added. After stirring the solution for 24 h the reaction mixture was analyzed by ^{31}P NMR. No formation of Et_3P=NMes (δ = 6.8 ppm) was observed. An authentic sample of Et_3P=NMes was prepared via the Staudinger reaction between PEt_3 and N_3Mes to confirm this signal. The signal at δ = −16.8 ppm belongs to the employed PEt_3.

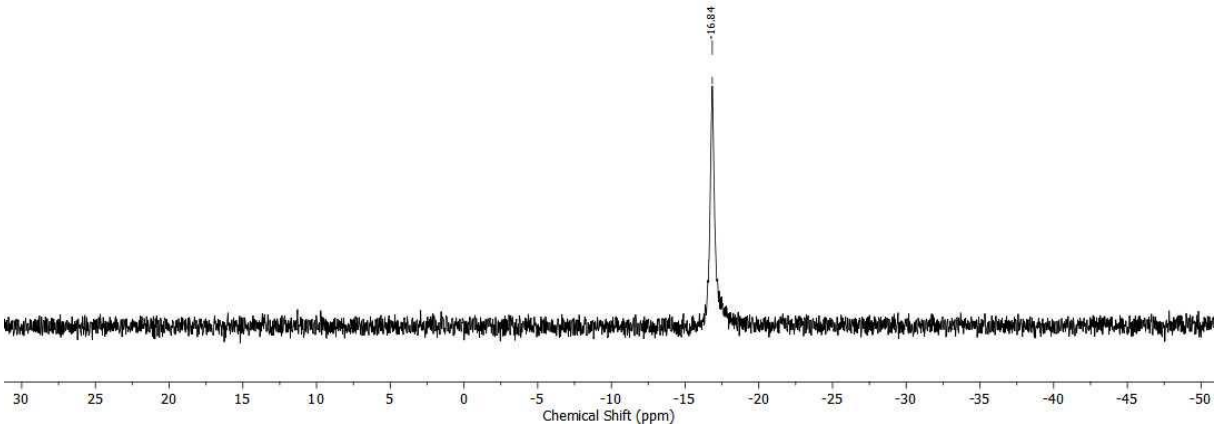

Figure S11. ^{31}P NMR spectrum of K{crypt.222}[Fe(NMes)(N{Dipp}$SiMe_3)_2$] (K{crypt.222}[**1**]) and 2 equiv. of PEt_3 in THF after 24 h (298 K, 250 MHz).

After addition of the stronger complex agent 2,2´-bipyridin (5 mg, 0.03 mmol, 1.3 equiv.) the solution was stirred for additional 24 h. No other signals besides that of PEt_3 could be observed by ^{31}P NMR spectroscopy (Figure S12).

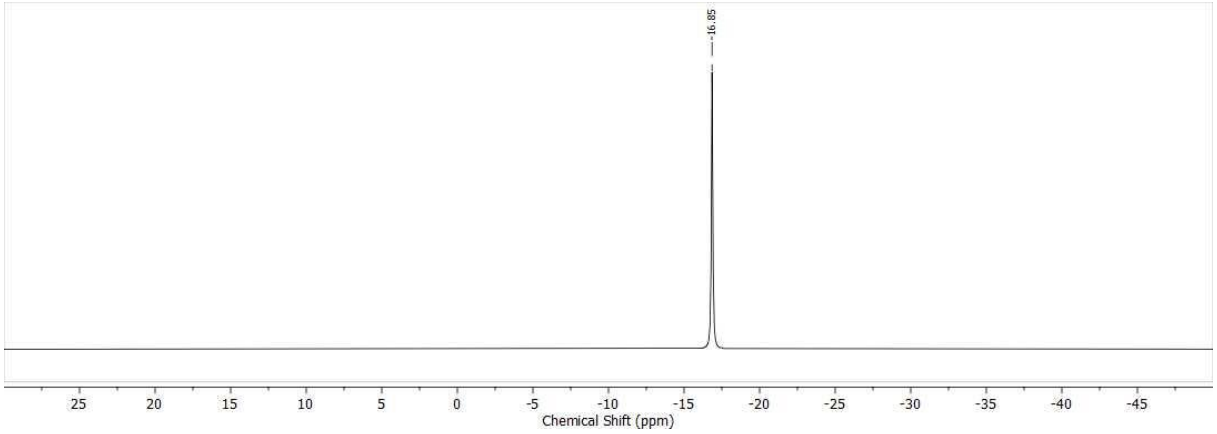

Figure S112. ^{31}P NMR spectrum of the abovementioned reaction mixture (K{crypt.222}[Fe(NMes)(N{Dipp}$SiMe_3)_2$] (K{crypt.222}[**1**]) and 2 equiv. of PEt_3 in THF-d_8) which was treated with 2,2'-bipyridin and measured again after 24 h (298 K, 250 MHz).

Independent reaction of Et_3P=NMes with [**1**]$^-$ or with the iron(II) silylamide K{crypt.222}[Fe(N{Dipp}$SiMe_3)_2$], resulting from a successful nitrene transfer of [**1**]$^-$ to PEt_3, gave no interactions by means of ^{31}P NMR spectroscopy.

Reaction of [1] with PEt_3

To a solution of 30 mg (0.04 mmol, 1 equiv.) [**1**], dissolved in 0.4 mL *n*-pentane, a second solution of 10 mg (0.08 mmol, 2 equiv.) PEt_3, dissolved in 0.2 mL *n*-pentane, was added. After stirring the solution for 24 h the reaction mixture was analyzed by ^{31}P NMR with no observable formation of $Et_3P{=}NMes$ (δ = 6.8 ppm). Only a very broad and small signal of the employed PEt_3 was observed (Figure S12), which is attributed to reversible binding of the phosphine to [**1**].

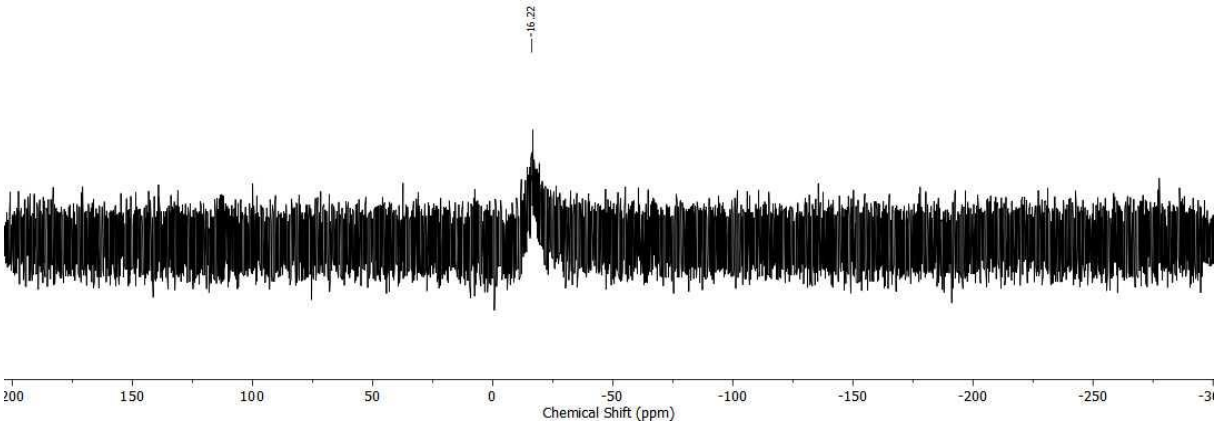

Figure S13. ^{31}P NMR spectrum of K{crypt.222}[Fe(NMes)(N{Dipp}$SiMe_3)_2$] (K{crypt.222}[**1**]) with added 2 equiv. of PEt_3 in THF-d_8 after 24 h(298 K, 250 MHz).

After addition of the stronger complex agent 2,2´-bipyridin (8 mg, 0.05 mmol, 1.3 equiv.) the reversible phosphine coordination is blocked with reoccurrence of a sharp signal for PEt_3 as well as observation of a signal at δ = 6.8 ppm that corresponds to $Et_3P{=}NMes$ (Figure S14).

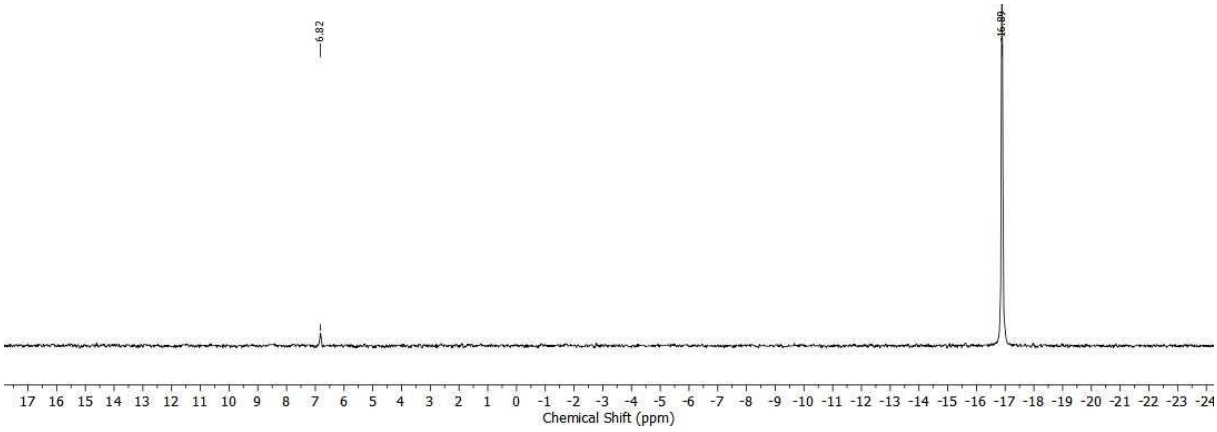

Figure S14. ^{31}P NMR spectrum of [Fe(N(NMes){Dipp}$SiMe_3)_2$] [**1**]) with added 2 equiv. of PEt_3 in THF-d_8 after 24 h(298 K, 250 MHz).

Independent reaction of $Et_3P{=}NMes$ with [**1**] or with the iron(II) silylamide [Fe(N{Dipp}$SiMe_3)_2$], resulting from a successful nitrene transfer of [**1**] to PEt_3, revealed no interactions by means of ^{31}P NMR spectroscopy.

Reactivity towards carbon monoxide

Reaction of K[{crypt.222}[1] with CO

30 mg (0.03 mmol, 1 equiv.) K{crypt.222}[**1**] were dissolved in 0.5 mL THF-d_8 in a *J*-Young NMR tube and 1 atm. CO was added. The green solution was analyzed by ^{1}H NMR spectroscopy after 24 h. Formation of MesNCO (integrated signals) is visible (Figure 15).[5]

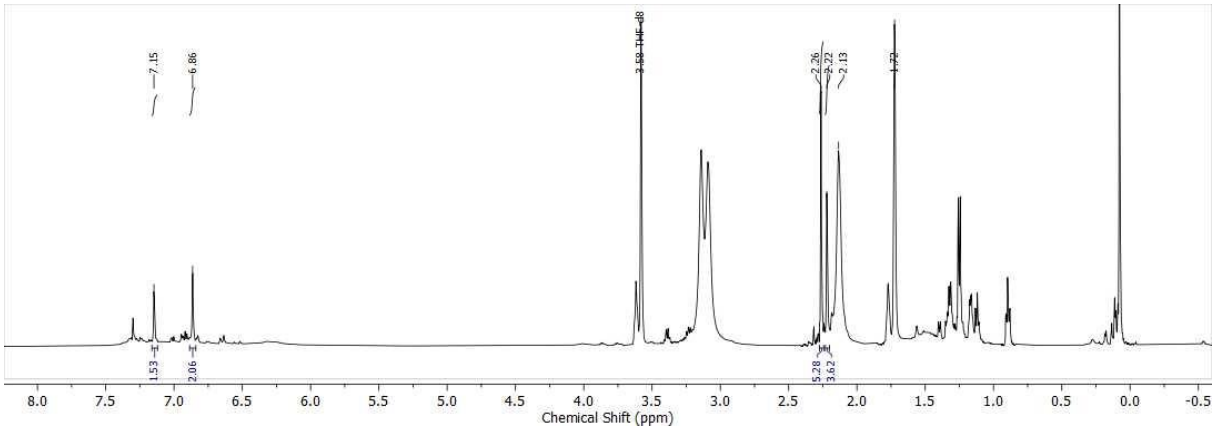

Figure S15. ^{1}H NMR spectrum of K{crypt.222}[Fe(NMes)(N{Dipp}SiMe$_3$)$_2$] (K{crypt.222}[**1**]) 24 h after addition of 1 atm. CO in THF-d_8 (298 K, 300 MHz).

Reaction of [1] with CO

30 mg (0.04 mmol, 1 equiv.) [**1**] were dissolved in 0.5 mL C_6D_6 in a *J*-Young NMR tube and 1 atm. CO was added. The brown solution was analyzed by ^{1}H NMR spectroscopy after 24 h (Figure S16) yielding only the signature of the employed [**1**].

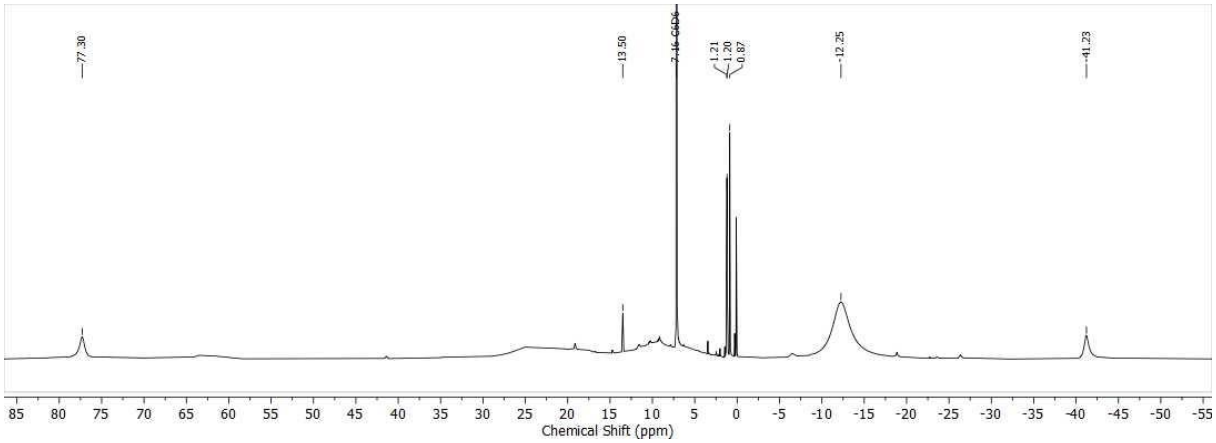

Figure S16. ^{1}H NMR spectrum of [Fe(NMes)(N{Dipp}SiMe$_3$)$_2$] ([**1**]) 24 h after addition of 1 atm CO in C_6D_6 after 24 h (298 K, 300 MHz).

Hydrogen atom transfer (HAT) reactivity

Reaction of K{crypt.222}[1] with 1,4-Cyclohexadiene

To a solution of 25 mg (0.02 mmol, 1 equiv.) K{crypt.222}[**1**], dissolved in 0.5 mL tetrahydrofuran-d_8, 4 mg (0.04 mmol, 2 equiv.) 1,4-CHD were added. After stirring the solution for 24 hours formation of benzene (δ = 7.30 ppm, 73 % conversion) was observed by ^{1}H NMR spectroscopy. Attempts for identification and isolation of the presumably resulting iron amide complex or any other iron containing reaction product via crystallisation was not successful.

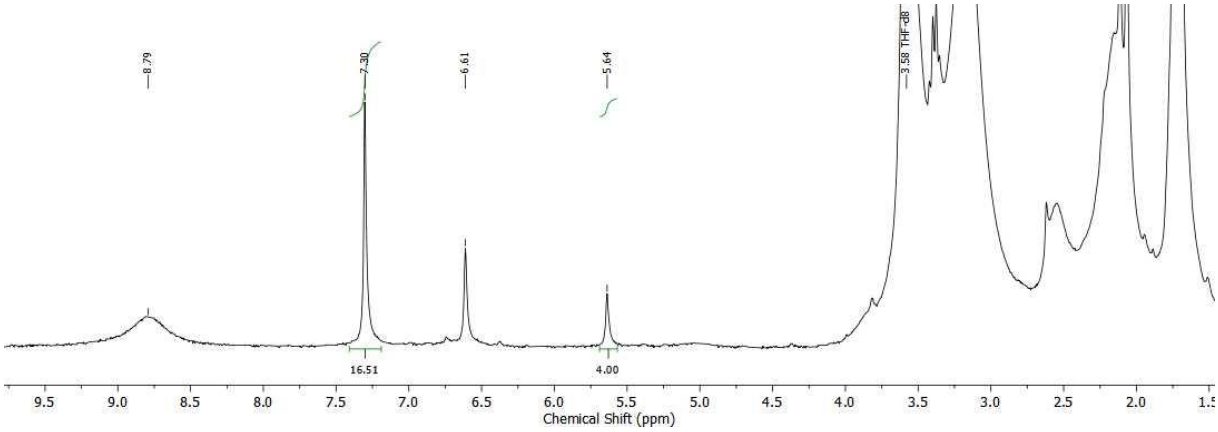

Figure S17. ^{1}H NMR spectrum of K{crypt.222}[Fe(NMes)(N{Dipp}SiMe$_3$)$_2$] (K{crypt.222}[**1**]) 24 h after addition of 2 equiv. 1,4-CHD in THF-d_8 (298 K, 300 MHz).

Reaction of [1] with 1,4-Cyclohexadiene

To a solution of 30 mg (0.04 mmol, 1 equiv.) [**1**], dissolved in 0.5 mL toluene-d_8, 7 mg (0.09 mmol, 2 equiv.) 1,4-CHD were added. After stirring the solution for 24 h formation of benzene (δ = 7.12 ppm, 39% conversion) was observed by ^{1}H NMR. Attempts for identification and isolation of the presumably resulting iron amide complex or any other iron containing reaction product via crystallisation was not successful.

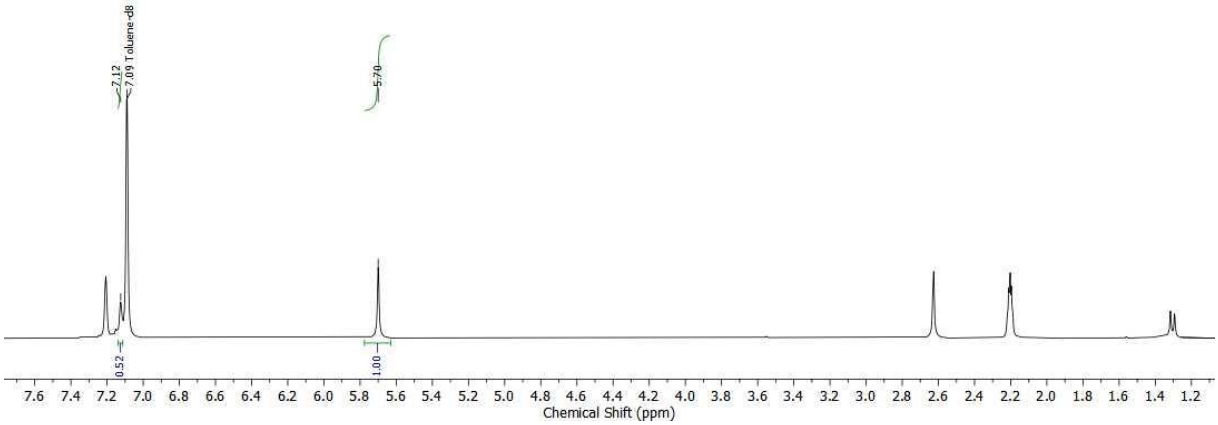

Figure S18. ^{1}H NMR spectrum of [Fe(NMes)(N{Dipp}SiMe$_3$)$_2$] ([**1**]) 24 h after addition of 2 equiv. 1,4-CHD in toluene-d_8 (298 K, 300 MHz).

Reaction of K{crypt.222}[1] with 1-Hydroxy-2,2,6,6-tetramethyl-piperidine (TEMPO-H)
To a solution of 30 mg (0.03 mmol, 1 equiv.) K{crypt.222}[**1**], dissolved in 0.5 mL THF-d_8, 4 mg (0.03 mmol, 1 equiv.) TEMPO–H were added. The conversion was analysed by ^{1}H NMR spectroscopy by calibrating TEMPO–H (δ = 1.08 ppm) versus the cryptand signal. The conversion amounted to 35% after 24 h (by ^{1}H NMR). Attempts for identification or isolation of the presumably formed iron amide or any other iron containing product was not successful.

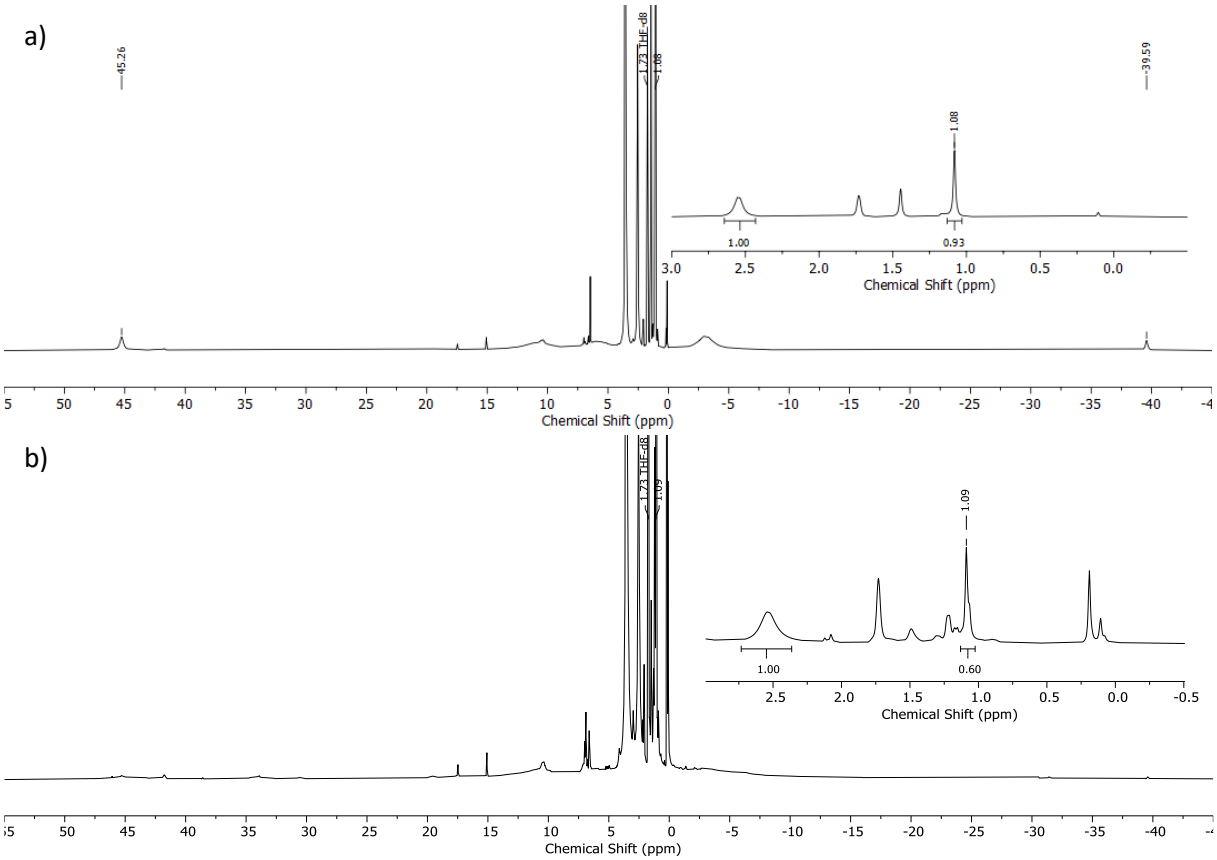

Figure S19. ^{1}H NMR spectra of K{crypt.222}[Fe(NMes)(N{Dipp}SiMe$_3$)$_2$] (K{crypt.222}[**1**]) in addition of 1 equiv. TEMPO–H in THF-d_8 after 15 min (a) and 24 h (b) (298 K, 300 MHz).

In addition to the NMR-experiment a mixture of 7 mg (0.01 mmol, 1 equiv.) K{crypt.222}[**1**] and 1 mg (0.01 mmol, 1 equiv.) of TEMPO–H, dissolved in 0.4 mL THF, was examined via X-Band EPR spectroscopy. The time-dependent graph shows initial formation of minor amounts of the TEMPO radical that vanish over time. Given the significant conversion of TEMPO-H by ^{1}H NMR spectroscopy (35% after 24 h) this indicates follow-up/side reactions of either TEMPO or TEMPO-H with either the formed amide or the employed imide.

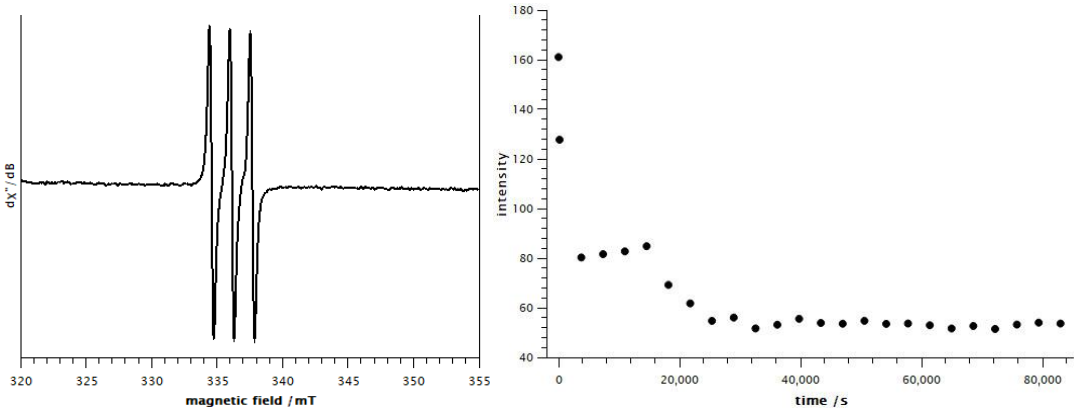

Figure S20. Left: X-Band EPR spectrum of K{crypt.222}[Fe(NMes)(N{Dipp}$SiMe_3$)$_2$] (K{crypt.222}[**1**]) with addition of 1 equiv. TEMPO–H in THF recorded after 10 min at 303.75 K (frequency 9.436407 GHz, 1.0 mW microwave power, 0.5 G modulation amplitude with 100 kHz modulation frequency). Right: Time dependence of the absolute intensity of the the EPR spectroscopic resonance due to the TEMPO radical, generated from the reaction of K{crypt.222}[**1**] with 1 equiv. TEMPO–H.

Reaction of [1] with 1-Hydroxy-2,2,6,6-tetramethyl-piperidine (TEMPO-H)

To a solution of 30 mg (0.04 mmol, 1 equiv.) [**1**], dissolved in 0.5 mL, C_6D_6 7 mg (0.04 mmol, 1 equiv.) TEMPO–H were added. The reaction was monitored by ^{1}H-NMR-spectroscopy.

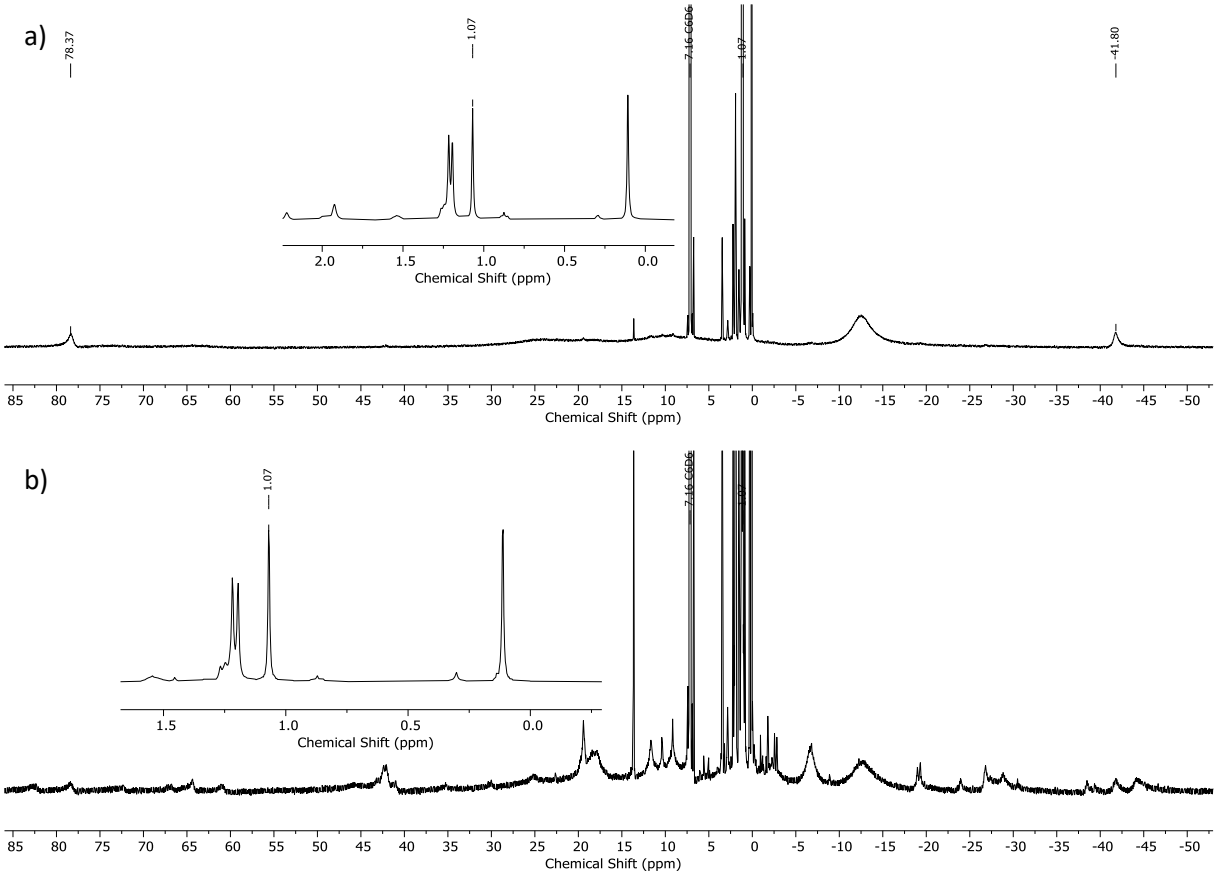

Figure S21. ^{1}H NMR spectra of [Fe(NMes)(N{Dipp}$SiMe_3$)$_2$] ([**1**]) treated with 1 equiv. TEMPO–H in toluene-d_8, measured after 15 min (a) and 24 h (b) (298 K, 300 MHz), showing the partial conversion of [**1**] and appearance of a set of signals ascribed to one or more paramagnetic species.

In addition to the NMR-spectroscopic experiments, EPR-spectroscopic examination of a solution of 4 mg (0.01 mmol, 1 equiv.) [**1**] and 1 mg (0.01 mmol, 1 equiv.) TEMPO–H in 0.4 mL toluene was carried out. The EPR spectroscopic resonance of TEMPO generated in this reaction is shown in Figure S22 (left); a plot showing the intensity of this signal as a function of the reaction time is shown in Figure S22 (right). In order to evaluate the amount of TEMPO generated in this reaction, an EPR spectroscopic calibration curve for the TEMPO radical was recorded, covering the relevant concentration range of the TEMPO radical (Figure S23). Using this calibration, the conversion of TEMPO–H to TEMPO reached 34% after 24 h. Only minor changes were observed after that (conversion of TEMPO–H to TEMPO after 47 h: 36%).

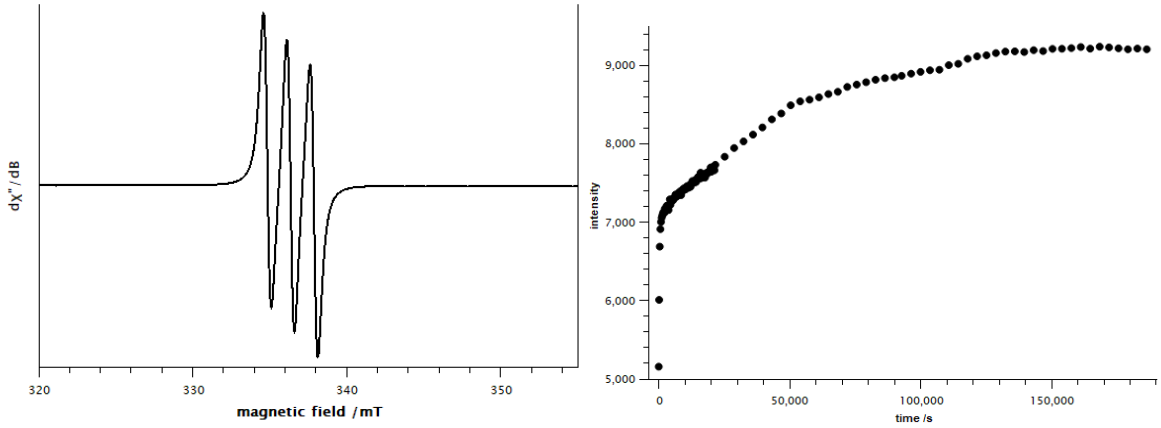

Figure S22. Left: X-Band EPR spectrum of [Fe(NMes)(N{Dipp}$SiMe_3$)$_2$] ([**1**]) 10 minutes after addition of 1 equiv. TEMPO–H in toluene (collected at 303.75 K (frequency 9.436407 GHz, 1.0 mW microwave power, 2 G modulation amplitude with 100 kHz modulation frequency). Right: Time dependence of the absolute EPR intensity of the TEMPO radical formed from the reaction of [Fe(NMes)(N{Dipp}$SiMe_3$)$_2$] ([**1**]) with 1 equiv. TEMPO–H.

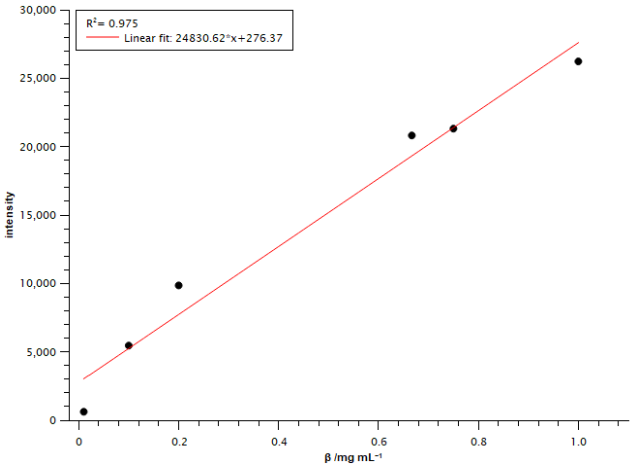

Figure S23. Calibration slope of absolute intensitiy of the EPR spectroscopic signal of TEMPO vs. the concentration of TEMPO in toluene (c = 0.01 mg/mL; 0.10 mg/mL; 0.20 mg/mL; 0.667 mg/mL; 0.75 mg/mL; 1.0 mg/mL).

Cyclic voltammetry

The redox behavior of K{crypt.222}[**1**] was examined by using a microcell HC “closed” stand (*rhd instruments*) in combination with a temperature controller (*rhd instruments*) and an *AUTOLAB PGSTAT 202* (*Metrohm GmbH*) potentiostat/galvanostat. The measurements were performed at 25±0.1 °C, using a *TSC 1600 Closed* (*rhd instruments*) Pt cell in a three electrode configuration with Pt wires acting as pseudo reference and as working electrode. The redox behaviour of [**1**] was examined by using a *TSC 1600 Closed* (*rhd instruments*) glassy carbon cell in a three-electrode configuration with an Ag wire acting as pseudo reference electrode and a glassy carbon working electrode. To secure reproducible conditions the electrodes were freshly polished, rinsed with THF and dried *in vacuo* for 2 hours. 2 mM of analyte and 0.1 M nBu$_4$N[PF$_6$], which acted as electrolyte, were used in the default measurement setup. The [FeCp$_2$] / [FeCp$_2$]$^+$ (Fc/Fc$^+$) redox couple was used as internal standard. The measurements were performed at four different scan rates (50, 100, 200, 500 mV/s), with two full cycles per scan rate. Peak potentials and currents of the second cycle of each measurement were determined using the *NOVA* Software (ver. 2.1.4, *Metrohm GmbH*).

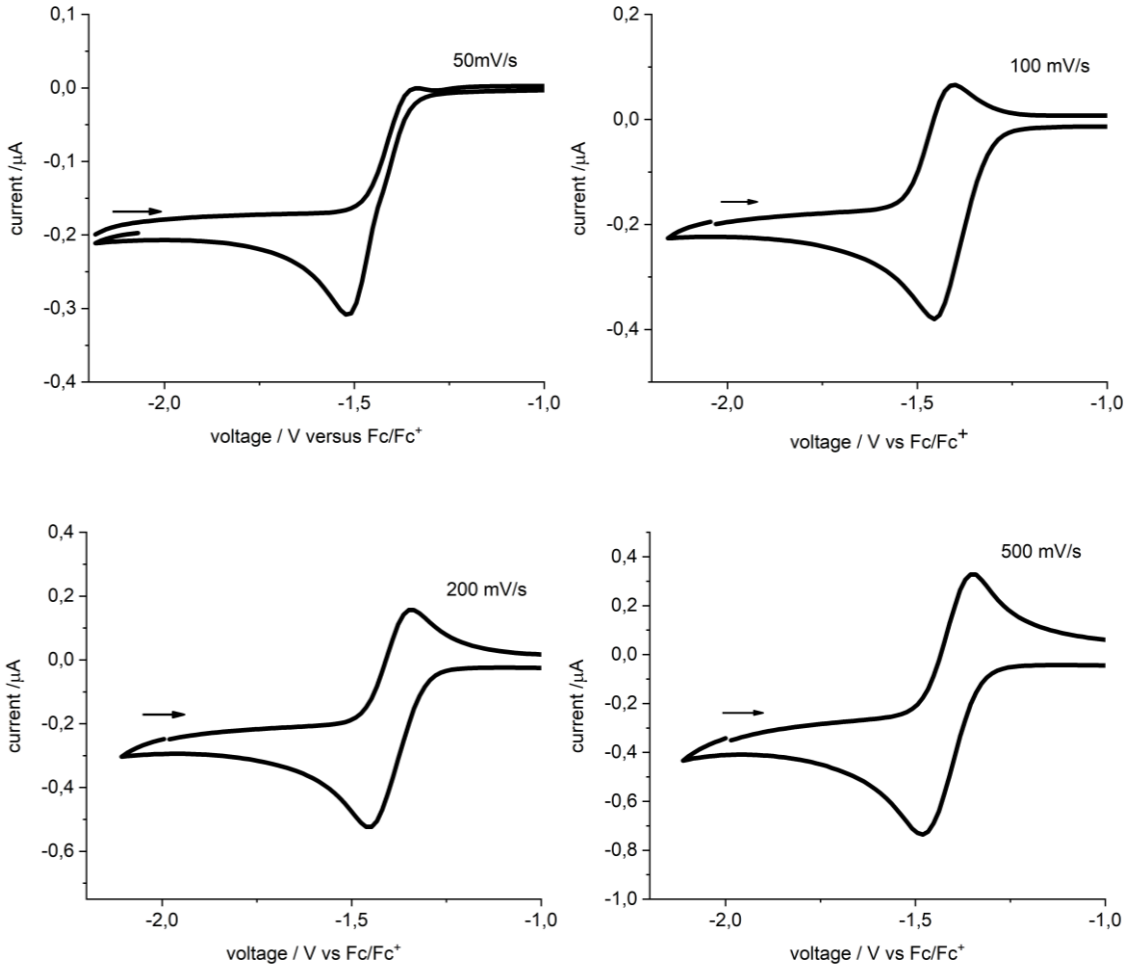

Figure S24. Cyclic voltammograms of K{crypt.222}[**1**] in THF at depicted scan rates (0.1 M nBu$_4$N[PF$_6$] vs Fc/Fc$^+$). The redox process at –1.40 V is assigned to the [**1**]$^-$ / [**1**] couple.

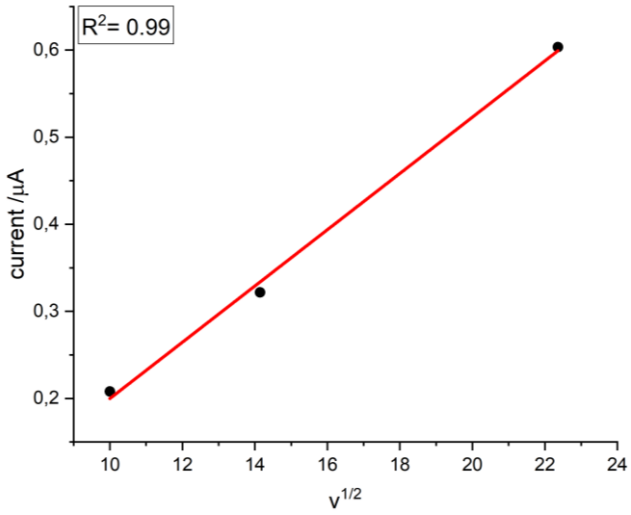

Figure S25. Randles-Sevcik fit for the electron transfer at $E_{1/2}$=−1.40 V of K{m}[**1**] in THF.

Table S1. Electrochemical data for the electron transfer at $E_{1/2}$=−1.40 V of K{crypt.222}[**1**] in THF.

Scan rate /mV/s	$E_{1/2}$ /V	I_{pa} /µA	I_{pc} /µA	$\lvert I_{pa}/I_{pc}\rvert$
50	−1.42	---	−0.25	---
100	−1.41	0.20	−0.31	1.49
200	−1.40	0.32	−0.43	1.33
500	−1.40	0.60	−0.62	1.03

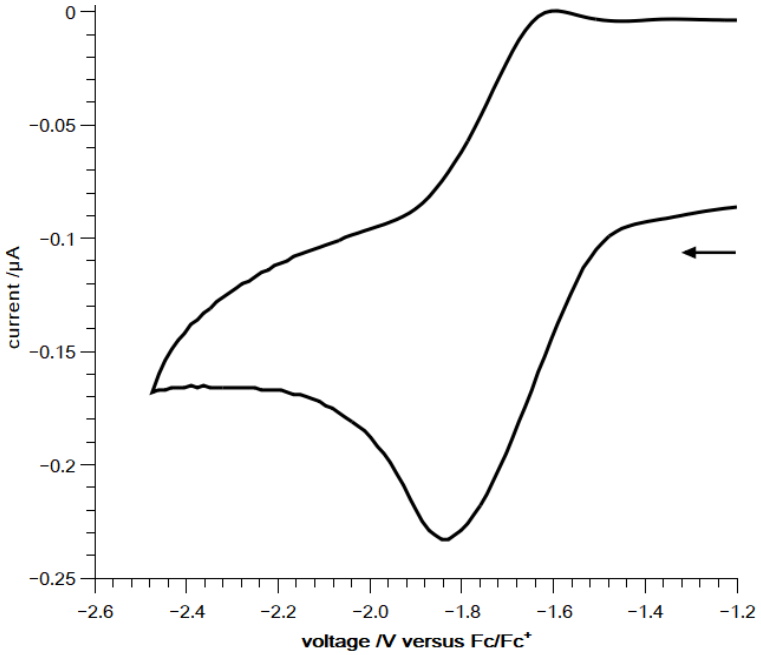

Figure S26. Section of the cyclic voltammogram of [**1**] in THF at a scan rate of 200 mV/s (0.1 M nBu$_4$N[PF$_6$] vs Fc/Fc$^+$). The reversible redox process is assigned to the [**1**]$^-$ / [**1**] couple.

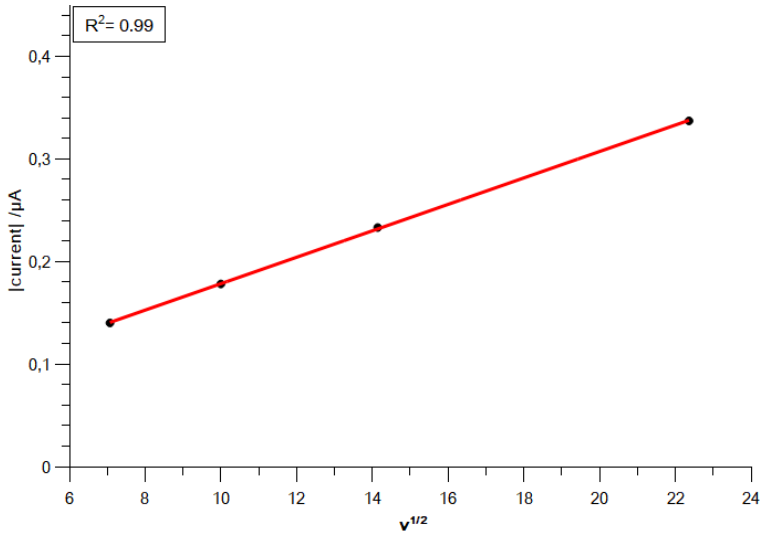

Figure S27. Randles-Sevcik fit for the electron transfer at $E_{1/2}$ = −1.72 V of [**1**] in THF.

Table S2. Electrochemical data for the electron transfer at $E_{1/2}$=−1.72 V of [**1**] in THF.

Scan rate /mV/s	$E_{1/2}$ /V	I_{pa} /µA	I_{pc} /µA	$\lvert I_{pa}/I_{pc}\rvert$
50	−1,74	0.053	−0.065	0.82
100	−1.70	0.072	−0.085	0.85
200	−1.72	0.13	−0.12	1.08
500	−1.71	0.21	−0.18	1.17

Mössbauer spectroscopy

Mössbauer spectra were recorded with a ^{57}Co source in a Rh matrix using an alternating constant acceleration Wissel Mössbauer spectrometer operated in the transmission mode and equipped with a Janis closed-cycle helium cryostat. Isomer shifts are given relative to iron metal at ambient temperature. Simulation of the experimental data was performed with the Mfit program using Lorentzian line doublets: E. Bill, Max-Planck Institute for Chemical Energy Conversion, Mülheim/Ruhr, Germany.

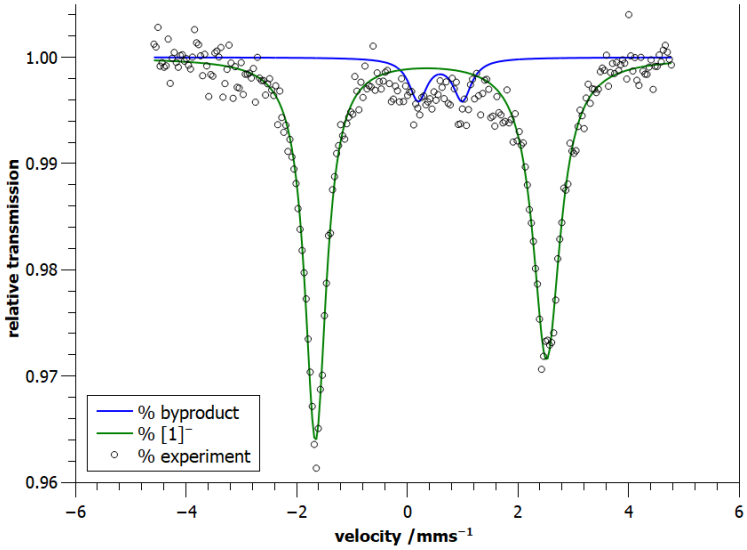

Figure S28. Zero field ^{57}Fe Mössbauer spectrum of solid K{crypt.222}[**1**] at 80 K. The green line represents a fit with δ = 0.43 mm/s, $|\Delta E_Q|$ = 4.18 mm/s, which can be assigned to K{crypt.222}[**1**] (91.4%). The blue line represents a fit with δ = 0.60 mm/s, $|\Delta E_Q|$ = 0.80 mm/s, which assigned to an unknown iron(II) byproduct (8.6%).

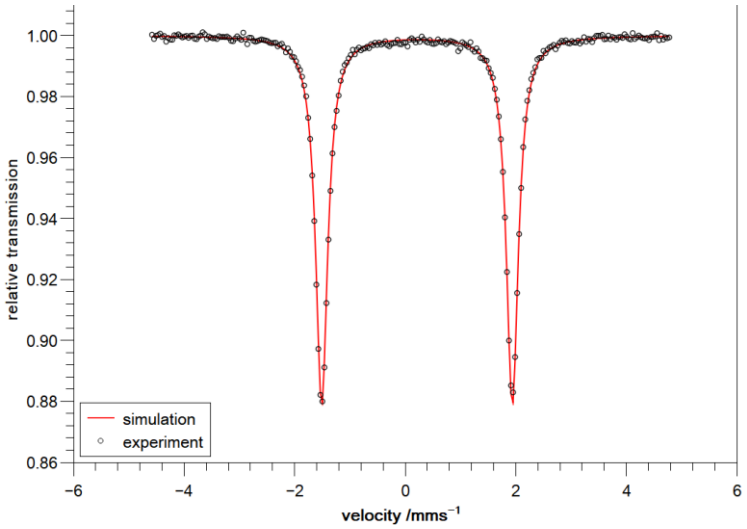

Figure S29. Zero field ^{57}Fe Mössbauer spectrum of solid [**1**] at 80 K. The red line represents a fit with δ = 0.21 mm/s, $|\Delta E_Q|$ = 3.45 mm/s, which can be assigned to [**1**].

Magnetic measurements

Temperature-dependent magnetic susceptibility measurements were carried out with a Quantum-Design MPMS3 SQUID magnetometer equipped with a 7 Tesla magnet in the range from 210 to 2.0 K at a magnetic field of 0.5 T. The powdered samples were contained in a polycarbonate capsule, covered with a few drops of low viscosity perfluoropolyether based inert oil Fomblin Y45 to fix the crystals, and fixed in a non-magnetic sample holder. Each raw data file for the measured magnetic moment was corrected for the diamagnetic contribution of the sample holder and the polycarbonate capsule. The molar susceptibility data were corrected for the diamagnetic contribution.

Experimental temperature dependent and VTVH (variable temperature – variable field) data were simultaneously modelled by using a fitting procedure to the appropriate Heisenberg-Dirac-van-Vleck (HDvV) spin Hamiltonian for Zeeman splitting and zero-field splitting, equation (1).

$$\widehat{H} = g\mu_B \vec{B}\vec{S} + D\left[\hat{S}_z^2 - \frac{1}{3}S(S+1)\right] \quad (1)$$

Simulation of the experimental magnetic data was performed with the julX_2s program: E. Bill, Max-Planck Institute for Chemical Energy Conversion, Mülheim/Ruhr, Germany.

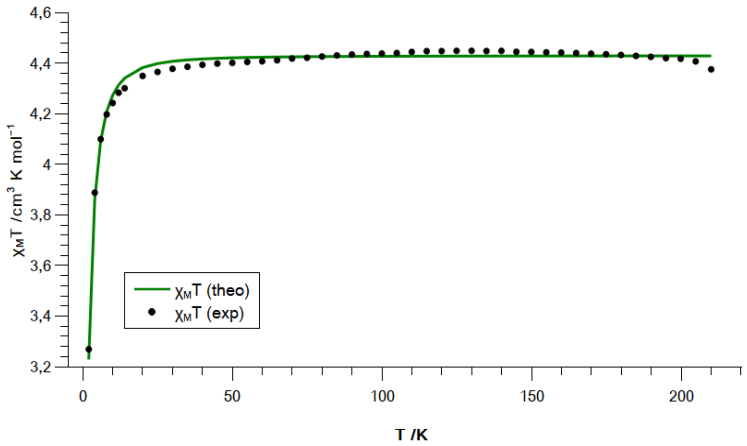

Figure S30. Plot of $\chi_M T$ vs temperature of K{crypt.222}[**1**] with an applied field B = 0.5 T. The green line represents the best fit with the parameters S = 5/2, D = 2.5 cm^{-1}, g = 2.01.

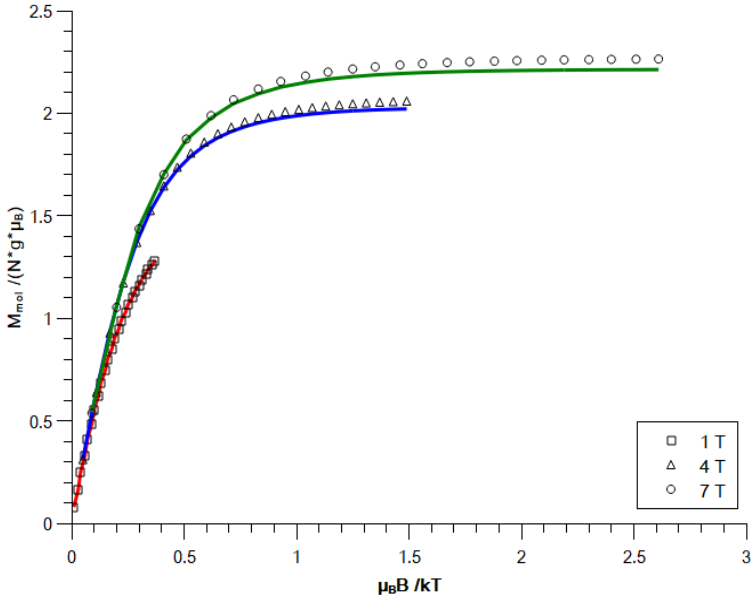

Figure S31. Plot of M_{mol} vs $\mu_B B$ of K{crypt.222}[**1**] with an applied field B = 1 T (red), 4 T (blue) 7 T(green). The lines represent the best fit with the parameters S = 5/2, D = 2.5 cm^{-1}, g = 2.01.

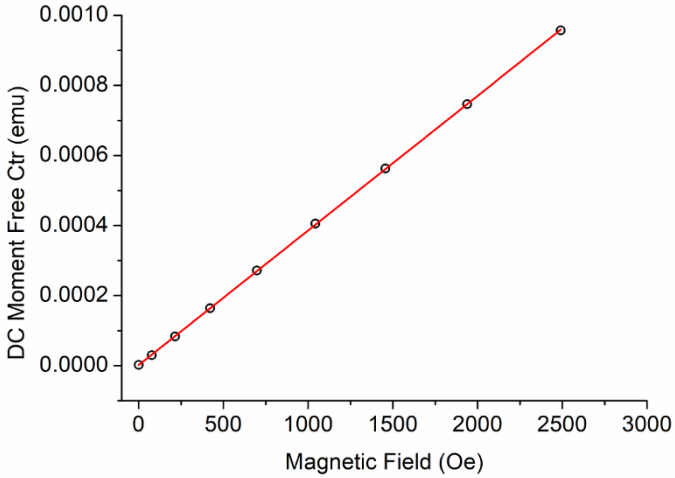

Figure S32. Moment vs. field measurement of K{crypt.222}[**1**] at 100 K. The linear behaviour (red line, goodness of linear correlation: Pearson R = 0.99999, R^2 = 0.99997) clearly indicates the absence of magnetic impurities/nanoparticles.

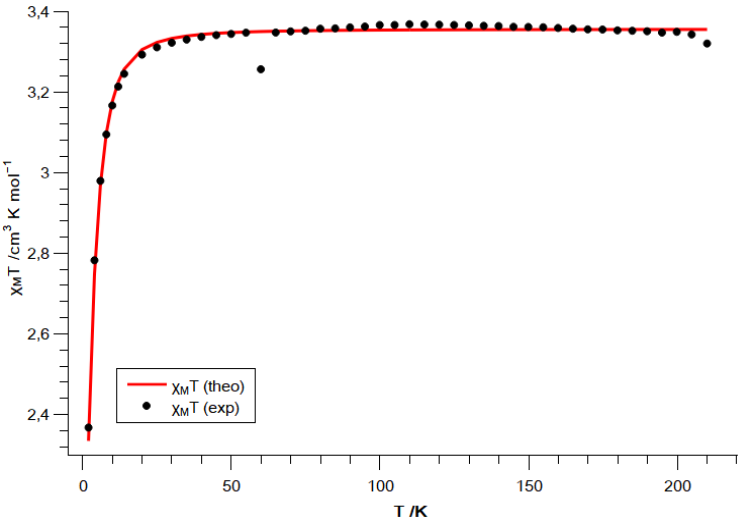

Figure S33. Plot of $\chi_M T$ vs temperature of [**1**] with an applied field B = 0.5 T. The red line represents the best fit with the parameters S = 2, D = −3.5 cm^{-1}, g = 2.12.

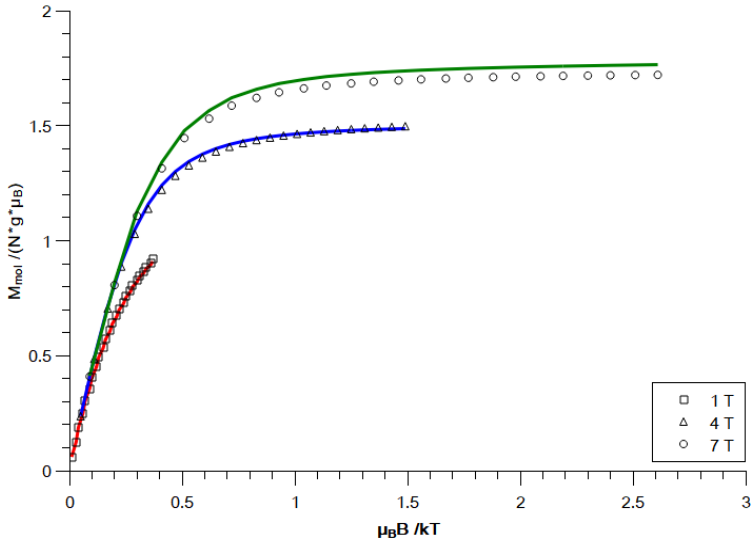

Figure S34. Plot of M_{mol} vs $\mu_B B$ of [**1**] with an applied field B = 1 T (red), 4 T (blue) 7 T(green). The lines represent the best fit with the parameters S = 2, D = −3.5 cm^{-1}, g = 2.12.

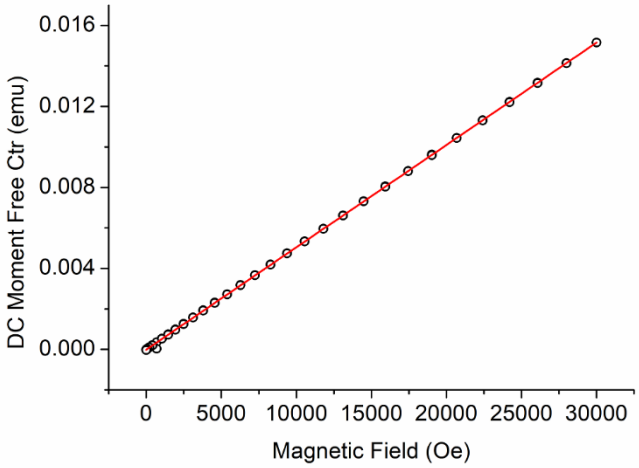

Figure S35. Moment vs. field measurement of [**1**] at 100 K. The linear behaviour (red line, goodness of linear correlation: Pearson R = 0.99996, R^2 = 0.99993) clearly indicates the absence of magnetic impurities/nanoparticles.

Electron-paramagnetic-resonance spectroscopy (EPR)

Helium-temperature EPR spectra were performed on a Bruker EMXplus (X-band) EPR spectrometer equipped with the Bruker ER4118X-MD5 probe head. The freshly prepared samples were transferred to J. Young quartz EPR tubes and sealed. The solution in the tube was frozen in liquid nitrogen and kept frozen until measured.

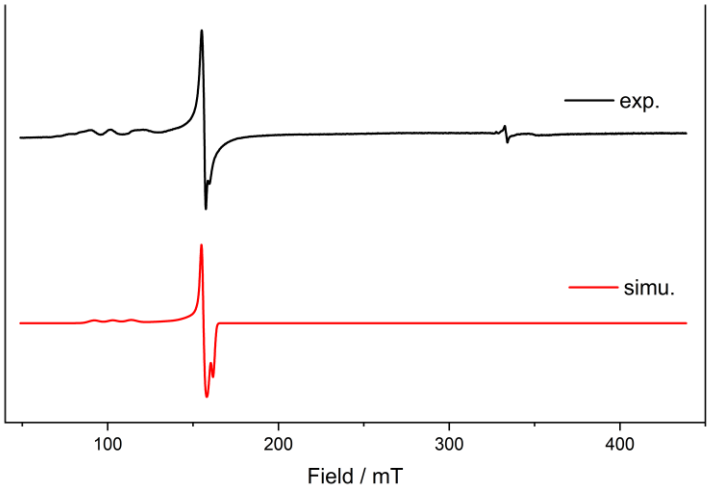

Figure S36. X-Band EPR spectrum of K{crypt.222}[**1**] in frozen THF (frequency 9.354709 GHz, 1.002 mW power, 4.996 G modulation amplitude) collected at 13.0 K (black). Simulation of data using the program EasySpin (red).[6] Fitting parameters: S = 5/2, g_1 = 6.5, g_2 = 4.28, g_3 = 4.18; A_1 = 349.69 G, A_2 = 3.57 G, A_3 = 42.82 G.

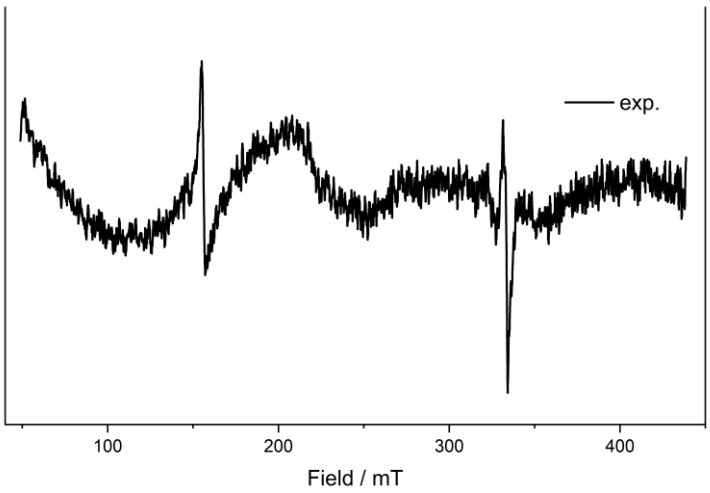

Figure S37. X-Band EPR spectrum of [**1**] in frozen *n*-hexane (frequency 9.359903 GHz, 1.002 mW power, 5 G modulation amplitude) collected at 12.97 K. The weak signals at g_1 = 4.3, g_2 = 2.0 are attributed to minimal amounts of an unknown iron(III) impurity.

Quantum chemical calculations

The calculations were performed with ORCA v. 5.0.1 and v. 5.0.2.[7] Three computational strategies were applied, relying either (1.) on the structural parameters from the solid-state structures, or (2) the structural parameters from the solid state in combination with truncation of bulky side-groups, or (3.) optimization of all structural parameters without any constraints. We have applied very similar computational protocols for the analysis of much related compounds.[8]

1. The positions of all hydrogen atoms were optimized (*optimizehydrogens true*) using the structural parameters from the solid-state structures and thus constraining the positions of all other atoms (PBE functional). Single point calculations were performed using the PBE,[9] PBE0,[10] and TPSSh,[11] functionals. Scalar relativistic effects were modeled under the Zeroth Order Regular Approximation (ZORA)[12] and the ZORA-def2-TZVPP[13] basis set. The D4[14] dispersion correction was used. The RI approximation with the related auxiliary basis sets (*SARC/J*)[15] were used to reduce computation time of calculations using the GGA functionals. For hybrid functionals, the RIJCOSX approximation was applied. Tighter-than-default scf (*tightscf*) criteria were applied. Mössbauer and EPR parameters were calculated following this approach. In case of the EPR calculations, 2nd order contribution to the HFCs from spin orbit coupling were considered (*aorb*). The calculation of the Mössbauer parameters followed the procedure developed by Björnsson *et al.* using the "full calibration parameter set" and consequently the functionals TPSSh, BP86 (instead of PBE) and B3LYP (instead of PBE0).[16]

2. The positions of all hydrogen atoms were optimized (*optimizehydrogens true*) using the structural parameters from the solid-state structures and thus constraining the positions of all other atoms (PBE functional). Additionally, the two Dipp groups were truncated by methyl groups. CASSCF/NEVPT2 calculations were then carried out at the triple-ζ level of theory (ZORA-def2-TZVPP, SARC/J, *autoaux, RIJCOSX*), with active spaces of (10,9) and (11,9) for [**1**] and [**1**]$^{-}$, respectively (Table S15).[17] The active space was chosen as to include d-orbitals, ligand centered orbitals and one set of aryl substituent centered π and π* orbitals (Fig. S76 – S80). Spin-orbit contributions were included by quasi-degenerate perturbation theory (QDPT). The electronic structure analysis in the main part of the manuscript relates to calculations without state averaging, whereas state-averaging was applied to determine the energies of vertically excited states.

3. This approach followed strategy (1), except that the structural parameters were optimized without constraints using the PBE, PBE0 and TPSSh functionals and the ZORA-def2-SVP basis set (def2-TZVP on Fe). All optimized structures were verified as true minima by the absence (N^{imag} = 0) of negative eigenvalues in the harmonic vibrational frequency analysis. Intrinsic bond orbitals (IBOs, Fig. 64)[18] were calculated at the triple-ζ level of theory and were visualized using Chemcraft and IBOview. The results obtained with PBE, TPSSh, PBE0 were consistent, with each functional giving rise to one strongly covalent orbital between the imido ligand and the metal. Following the amount of exact exchange, PBE slightly favors a d^5, *i.e.* Fe^{III} description for **[1]**, whereas TPSSh and PBE0 slightly favor a d^6, *i.e.* Fe^{II}, electron configuration (*vide infra*).

Table S3. Comparison of experimental (XRD) and computed (TPSSh, PBE, PBE0) bond lengths and angles of [**1**]$^-$ and [**1**].

	[**1**]$^-$				[**1**]			
	XRD	TPSSh	PBE	PBE0	XRD	TPSSh	PBE	PBE0
Fe–N_{imido} /Å	1.774	1.767	1.767	1.760	1.741	1.738	1.72	1.764
Fe–N_{amido} /Å	1.955	1.944	1.935	1.959	1.900	1.876	1.874	1.882
N–C_{Mes} /Å	1.339	1.336	1.335	1.332	1.337	1.331	1.342	1.315
N–Fe–N /°	115.0	113.3	112.4	114.2	114.3	115.8	117.5	114.4
Fe–N_{imido}–C /°	173.6	179.5	173.8	179.2	177.5	173.0	173.1	173.5

Table S4. Calculated Mössbauer parameters.

	Functional	ΔE **[mm s^{-1}]**	δ **[mm s^{-1}]**
[1]	Exp.	3.45	0.21
[1]$^-$	Exp.	4.17	0.43
[1]	BP86	2.64	0.29
[1]$^-$	BP86	3.86	0.38
[1]	TPSSh	2.98	0.78
[1]$^-$	TPSSh	3.95	0.88
[1]	B3LYP	3.25	0.26
[1]$^-$	B3LYP	4.05	0.37

Table S5. Spectroscopic parameters obtained by DFT methods. *A*-values are given in [MHz].

	g_x	g_y	g_z	A_x (Fe)	A_y (Fe)	A_z (Fe)	A_x (N_{imido})	A_y (N_{imido})	A_z (N_{imido})
TPSSh//Hopt									
[1]$^-$	2.01	2.01	2.02	4.8	5	8.1	6.3	16.8	9.1
[1]	2.01	2.02	2.02	10.3	11.1	11.5	20.8	10.6	-3.3
PBE//Hopt									
1]$^-$	2.01	2.01	2.02	5.9	6.7	8	6.5	15.4	9
[1]	2.01	2.01	2.02	10	11.7	13.6	21.4	11	2.1
PBE0//Hopt									
1]$^-$	2	2.01	2.02	-4.3	-4.6	-0.5	7.3	18	9.8
[1]	2	2.01	2.02	-1	0.5	0.8	19.8	11.6	-5.5
TPSSh//TPSSh									
[1]$^-$	2.01	2.01	2.02	3.6	3.7	6.6	6.3	16.7	9.2
[1]	2.01	2.01	2.02	10.3	11.2	11.6	19.7	9.7	11.6
Experimental									
[1]$^-$	6.5	4.28	4.18	/	/	/	980	10	120

Table S6. Spectroscopic parameters obtained by QDPT/NEVPT2/CASSCF. *A*-values are given in [MHz], *D*- and *E/D*-values in [cm^{-1}].

	g_x	g_y	g_z	A_x (Fe)	A_y (Fe)	A_z (Fe)	A_x (N_{imido})	A_y (N_{imido})	A_z (N_{imido})	*D*	*E/D*
[1]$^-$	2.00	2.00	2.04	18.1	-10.6	22.5	2.1	10.5	-2.8	-0.7	0.186
[1]	2.00	2.00	2.02	13.0	18.8	7.5	21.2	-7.8	1.8	-1.3	0.168

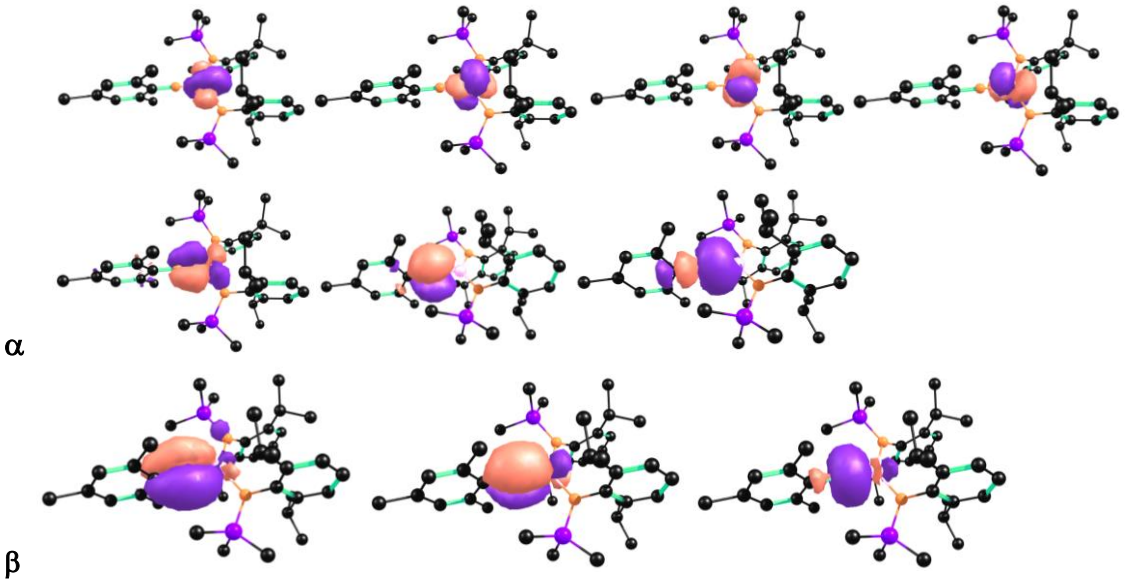

Figure S38. Metal-involving IBOs of [**1**] (TPSSh//TPSSh).

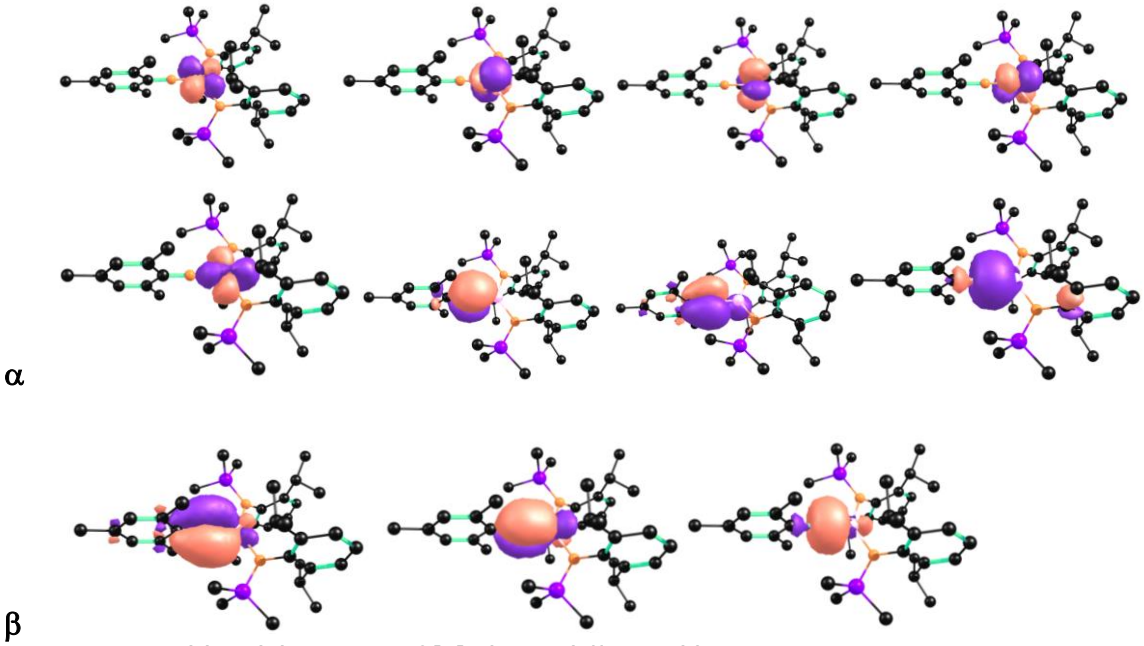

Figure S39. Metal-involving IBOs of [**1**]$^-$ (TPSSh//TPSSh).

0.62844 [1520]: 222111100
0.20752 [1485]: 221111110
0.12910 [1425]: 220111120
0.01176 [967]: 121211110
0.01052 [1139]: 202111102
0.00349 [1079]: 201111112
0.00274 [1282]: 211111111

Figure S40. Configuration of ground state of [**1**] as obtained by CASSCF(10,9).

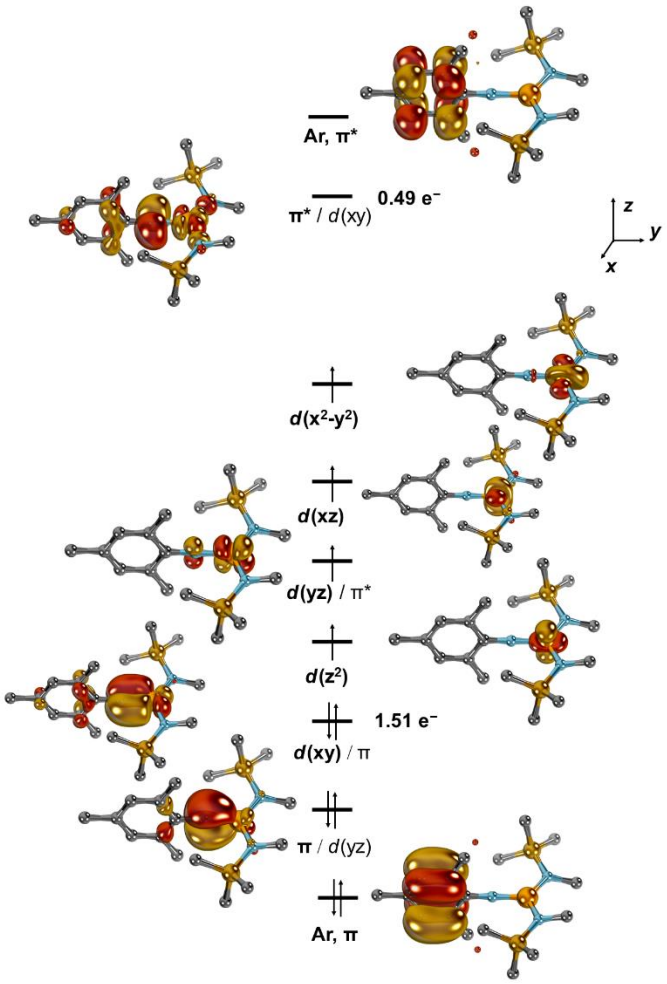

Figure S41. Entire active space [CASSCF(10,9)] of [**1**].

	101
	-0.42746
	1.98460
0 Fe px	2.5
0 Fe dxz	15.2
0 Fe dxy	0.0
1 Si pz	0.0
3 N px	0.9
4 N px	0.7
4 N py	0.0
5 N px	65.1
5 N py	0.0
7 C py	0.1
7 C dxz	6.8
8 C py	0.0
11 C py	0.0
12 C py	0.0
14 C py	0.0
18 C pz	0.0
22 C pz	0.0
34 C pz	0.0
34 C py	0.0

	102	103	104	105	106	107
	-0.33435	-0.34266	-0.25877	-0.23660	-0.24808	-0.27142
	1.96387	1.50792	1.01458	1.00012	1.00003	0.99988
0 Fe dz2	0.0	0.1	0.1	34.4	6.5	49.3
0 Fe dxz	0.0	0.0	89.5	0.0	0.0	0.0
0 Fe dyz	0.0	53.3	0.0	0.1	0.0	0.0
0 Fe dx2y2	0.0	0.0	0.0	33.6	15.0	45.1
0 Fe dxy	0.0	0.0	0.0	22.9	71.2	0.7
5 N px	0.0	0.0	6.5	0.0	0.0	0.0
5 N py	0.0	26.9	0.0	0.0	0.0	0.0
6 C py	17.1	2.1	0.0	0.0	0.0	0.0
8 C py	20.9	0.0	0.0	0.0	0.0	0.0
10 C py	18.1	2.1	0.0	0.0	0.0	0.0
12 C py	22.2	0.0	0.0	0.0	0.0	0.0

	108	109
	-0.03627	0.17939
	0.49289	0.03612
0 Fe s	0.0	0.0
0 Fe px	0.0	0.0
0 Fe dyz	45.7	0.0
0 Fe dx2y2	0.0	0.0
5 N py	33.4	0.0
6 C py	2.7	17.9
8 C py	0.1	15.4
9 H s	0.0	0.0
10 C py	2.6	19.0
11 C dxy	0.0	5.2
12 C py	0.0	16.7
13 H s	0.0	0.0
47 H s	0.1	0.0
48 H s	0.0	0.0
49 H s	0.0	0.0

Figure S42. Reduced Löwdin's population analysis of active space in CASSCF(10,9) of [**1**].

0.87647 [539]: 222111110
0.08912 [465]: 211221110
0.00964 [50]: 022111112
0.00431 [497]: 220111112
0.00340 [455]: 211211111
0.00268 [305]: 121121111

Figure S43. Configuration of ground state of [**1**]$^{-}$ as obtained by CASSCF(11,9).

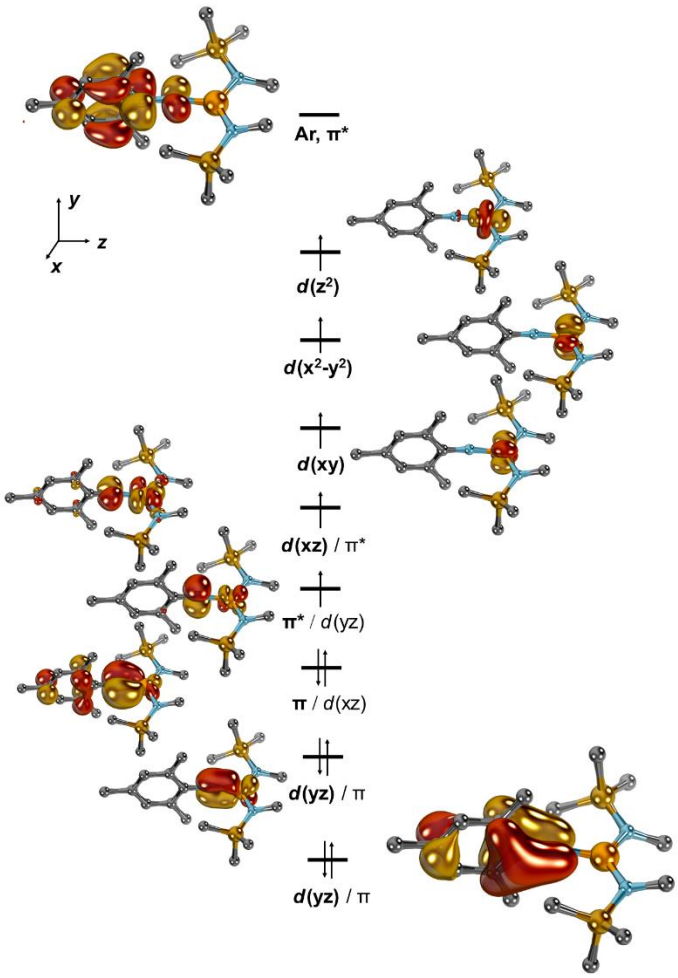

Fig. S44. Entire active space [CASSCF(11,9)] of [**1**]$^{-}$.

	101
	-0.27499
	1.96611
3 N px	5.4
3 N py	0.0
4 N pz	0.2
4 N px	17.4
4 N py	0.0
5 N px	0.1
6 C px	0.0
7 C px	0.0
9 C px	0.0
10 C px	0.0
11 C px	0.0
17 C px	0.0
26 C px	6.1
38 C py	0.6
42 C pz	5.5
46 C px	8.7

	102	103	104		105		106		107
	-0.28652	-0.18343		-0.01719		0.02489		0.02159		0.02643
	1.90056	1.88622		1.09936		1.09658		1.00006		1.00005
0 Fe dxz	0.6	22.0	0.1		73.4			0.0		0.0
0 Fe dyz	67.5	0.3	35.1			0.0		0.0		0.0
0 Fe dx2y2	0.0	0.0	0.0		0.0		6.7		86.3	
0 Fe dxy	0.0	0.0	0.0		0.0		89.2		7.1	
5 N px	0.6	40.7		0.3		11.1		0.0		0.0
5 N py	24.3	0.5	49.7			0.1		0.0		0.0
6 C dxz	0.1	5.6	0.0		1.9		0.0		0.0	
6 C dyz	2.1	0.1	5.6		0.0		0.0		0.0	
9 C px	0.0	5.4	0.1		1.2		0.0		0.0	
10 C px	0.0	5.7	0.2		1.2		0.0		0.0	
17 C px	0.0	5.7	0.1		1.3		0.0		0.0	

	108	109
	0.06099	0.33923
	1.00000	0.05106
0 Fe s	0.5	0.0
0 Fe dz2	89.2	0.0
5 N px	0.0	13.0
6 C px	0.0	34.2
7 C px	0.0	2.1
8 H s	0.0	0.0
9 C px	0.0	3.9
10 C px	0.0	4.9
11 C px	0.0	1.5
12 H s	0.0	0.0
17 C px	0.0	11.2
31 H s	0.0	0.0
32 H s	0.0	0.1
33 H s	0.0	0.3

Figure S45. Reduced Löwdin's population analysis of active space in CASSCF(11,9) of [**1**]$^{-}$.

Table S7. Covalency of π-bonds in **[1]$^{-}$** according to Löwdin's population analysis of the CASSCF(11,9) calculations.

	Fe	**N**
d(yz)/π	68	20
π/d(xz)	22	41
π*/d(yz)	35	50
d(xz)/π*	73	11

Table S8. Energies as obtained by strategy 1. Values are given in [Eh].

	Functional	***E***	***G***	***E*(SP)**
[**1**]$^-$	PBE	-3544.58506	-3543.76372	-3546.51764
[**1**]	PBE	-3544.50905	-3543.68365	-3546.43757
[**1**]$^-$	TPSSh	-3547.59864	-3546.75085	-3549.53167
[**1**]	TPSSh	-3547.51509	-3546.66455	-3549.44507
[**1**]$^-$	PBE0	-3544.84374	-3543.98957	-3546.77083
[**1**]	PBE0	-3544.75381	-3543.89704	-3546.67833

Table S9. Vertical energy gaps between *S* = 5/2 (ferromagnetically coupled) and *S* = 3/2 (antiferromagnetically coupled) states of **[1]**$^-$ as obtained by the PBE, TPSSh and PBE0 functionals or CASSCF/NEVPT2 (strategy 1). Negative energy differences ΔE indicate ferromagnetic coupling.

	ΔE in [eV]	***Löwdin's spin density on Fe of S = 5/2 state* in [a.u.]**	***Löwdin's spin density on imido nitrogen atom of S = 5/2 state* in [a.u.]**	***J* in [cm^{-1}]**
PBE	0.05	3.61	0.52	−93
TPSSh	−0.01	3.74	0.54	+13
PBE0	−0.08	3.85	0.54	+151
saCASSCF/ NEVPT2	−0.18	3.98	0.66	n.a.

Table S10. Electronic structure of broken-symmetry states of **[1]**$^-$ as obtained by the PBE, TPSSh and PBE0 functionals or CASSCF/NEVPT2 (strategy 1). Negative energy differences ΔE indicate ferromagnetic coupling. UCO = unrestricted corresponding orbitals.

	ΔE in [eV]	***Löwdin's spin density on Fe of "broken symmetry" state* in [a.u.]**	***Löwdin's spin density on imido nitrogen atom of "broken symmetry" state* in [a.u.]**	***UCO overlap***	**Assignment of „broken sym-metry" state**
PBE	+0.05	+2.74	+0.06	0.92	Fe^{I} nitrene (LMCT state)
TPSSh	−0.01	+3.09	−0.14	0.77	Fe^{II} imidyl
PBE0	−0.08	+3.34	−0.28	0.6	Fe^{II} imidyl
saCASSCF/ NEVPT2	−0.18	+3.37	−0.31	n.a.	Fe^{II} imidyl

Table S11. Vertical energy gaps between *S* = 5/2 (ferromagnetically coupled) and *S* = 3/2 (antiferromagnetically coupled) states of **[1]**$^-$ as obtained by the PBE, TPSSh and PBE0 functionals (strategy 3). Negative energy differences ΔE indicate ferromagnetic coupling.

	ΔE in [eV]	***Löwdin's Spin Density on Fe of S = 5/2 state* in [a.u.]**	***Löwdin's Spin Density on imido nitrogen atom of S = 5/2 state* in [a.u.]**	***J* in [cm^{-1}]**
PBE	−0.14	+3.62	+0.51	+230
TPSSh	−0.18	+3.76	+0.54	+311
PBE0	−0.22	+3.87	+0.54	+411

Table S12. Electronic structure of broken-symmetry states of **[1]**$^-$ as obtained by the PBE, TPSSh and PBE0 functionals (strategy 3). Negative energy differences ΔE indicate ferromagnetic coupling. UCO = unrestricted corresponding orbitals.

	Δ*E* in [eV]	***Löwdin's Spin Density on Fe of "broken symmetry" state in [a.u.]***	***Löwdin's Spin Density on imido nitrogen atom of "broken symmetry state"* in [a.u.]**	***UCO overlap***	**Assignment of „broken symmetry" state**
PBE	−0.14	+2.78	+0.05	0.90	Fe^{I} nitrene (LMCT state)
TPSSh	−0.18	+3.15	−0.15	0.75	Fe^{II} imidyl
PBE0	−0.22	+3.38	−0.28	0.60	Fe^{II} imidyl

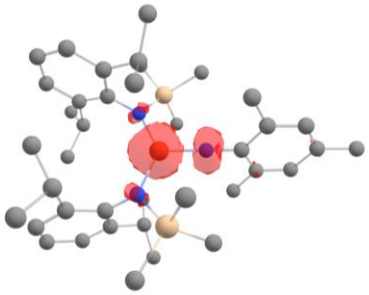

Figure S46. Spin-Density Distribution of *S* = 5/2 ground state of **[1]**$^{-}$ according to calculations using the TPSSh functional (strategy 1).

X-Ray diffraction analysis and molecular structures

Data for K{crypt.222}[Fe(N{Dipp}$SiMe_3)_2$] (CCDC 2130486), K{crypt.222}[**1**] (CCDC 2130485), [**1**] (CCDC 2130488) and K{crypt.222}[**2**] (CCDC 2130487) were collected at 100 K on a Bruker Quest D8 diffractometer using a graphite-monochromated Mo-K λ radiation (λ = 0.71073Å) and equipped with an *Oxford Instrument Cooler Device.* The structures have been solved using either OLEX SHELXT V2014/1 [xix] and refined by means of least-squares procedures on a F^2 with the aid of the program SHELXL-2016/6 [ii] include in the software package WinGX version 1.63[xx] or using CRYSTALS.[xxi] The Atomic Scattering Factors were taken from *International Tables for X-Ray Crystallography*.[xxii] All non-hydrogen atoms were refined anisotropically. All hydrogens atoms were refined by using a riding model. Absorption corrections were introduced by using the MULTISCAN and X-Red program.[xxiii, ix] Drawings of molecules are performed with the programs DIAMOND and POV-Ray with 50% probability displacement ellipsoids for non-H atoms. Depiction of H atoms is generally omitted for clarity.

Table S12. Crystal data and structure refinement for K{crypt.222}[Fe(N{Dipp}SiMe$_3$)$_2$].

Identification code	K_crypt_FeNDippTMS
Empirical formula	$C_{48}H_{88}FeKN_4O_6Si_2$
Formula weight / g mol^{-1}	968.35
Temperature / K	100.0
Crystal system	monoclinic
Space group	$P2_1/n$
a / Å	18.2810(8)
b / Å	14.0555(6)
c / Å	22.1239(9)
α / °	90
β / °	106.2980(10)
γ / °	90
V / Å^3	5456.3(4)
Z	4
ρ_{calc} / g cm^{-3}	1.179
μ / mm^{-1}	0.443
F(000)	2100.0
Crystal size / mm^3	0.499 × 0.411 × 0.214
Radiation	MoKα (λ = 0.71073)
2Θ range for data collection / °	4.468 to 53.59
Index ranges	−23 ≤ *h* ≤ 22, −17 ≤ *k* ≤ 17, −28 ≤ *l* ≤ 28
Reflections collected	114411
Independent reflections	11654 [R_{int} = 0.0456, R_{sigma} = 0.0232]
Data/restraints/parameters	11654/23/507
Goodness-of-fit on F^2	1.027
Final *R* indexes [*I*≥2σ (*I*)]	R_1 = 0.0422, wR_2 = 0.0955
Final *R* indexes [all data]	R_1 = 0.0548, wR_2 = 0.1020
Largest diff. peak/hole / e Å^{-3}	0.64/−0.53

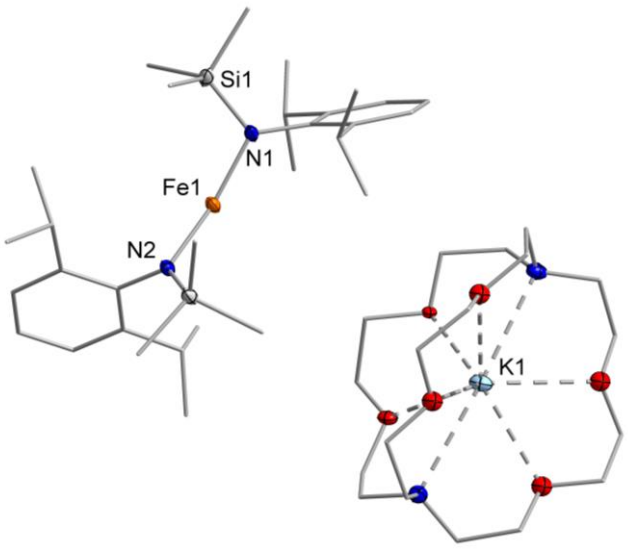

Figure S47. Molecular structure of K{crypt.222}[Fe(N{Dipp}SiMe$_3$)$_2$] within the crystal.

Table S13. Crystal data and structure refinement for [**1**].

Identification code	FeNMes_1
Empirical formula	$C_{39}H_{63}FeN_3Si_2$
Formula weight / g mol^{-1}	685.95
Temperature / K	100
Crystal system	orthorhombic
Space group	$Pbca$
a / Å	19.2646(7)
b / Å	16.7587(7)
c / Å	24.9520(11)
α / °	90
β / °	90
γ / °	90
V / Å^3	8055.7(6)
Z	8
ρ_{calc} / g cm^{-3}	1.131
μ / mm^{-1}	0.462
F(000)	2976.0
Crystal size / mm^3	0.22 × 0.144 × 0.111
Radiation	MoKα (λ = 0.71073)
2Θ range for data collection / °	3.89 to 49.994
Index ranges	−22 ≤ *h* ≤ 22, −19 ≤ *k* ≤ 19, −29 ≤ *l* ≤ 29
Reflections collected	76439
Independent reflections	7090 [R_{int} = 0.1078, R_{sigma} = 0.0499]
Data/restraints/parameters	7090/0/423
Goodness-of-fit on F^2	1.042
Final *R* indexes [*I*≥2σ (*I*)]	R_1 = 0.0464, wR_2 = 0.0897
Final *R* indexes [all data]	R_1 = 0.0651, wR_2 = 0.0952
Largest diff. peak/hole / e Å^{-3}	0.25/−0.29

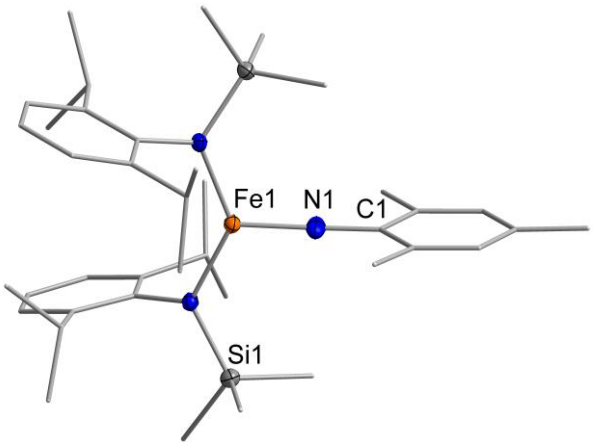

Figure S48. Molecular structure of [**1**] within the crystal.

Table S14. Crystal data and structure K{crypt.222}[**1**].

Identification code	K_crypt_1
Empirical formula	$C_{57}H_{99}FeKN_5O_6Si_2$
Formula weight / g mol^{-1}	1101.54
Temperature / K	100.00
Crystal system	monoclinic
Space group	$P2_1/c$
a / Å	11.9424(4)
b / Å	24.7899(9)
c / Å	22.9964(9)
α / °	90
β / °	95.9740(10)
γ / °	90
V / Å^3	6771.1(4)
Z	4
ρ_{calc} / g cm^{-3}	1.081
μ / mm^{-1}	0. 365
F(000)	2388.0
Crystal size / mm^3	0.21 × 0.14 × 0.13
Radiation	MoKα (λ = 0.71073)
2Θ range for data collection / °	3.922 to 56.616
Index ranges	$-15 \le h \le 15$, $-33 \le k \le 33$, $-30 \le l \le 28$
Reflections collected	85806
Independent reflections	16789 [R_{int} = 0.0388, R_{sigma} = 0.0346]
Data/restraints/parameters	16789/0/666
Goodness-of-fit on F^2	1.047
Final *R* indexes [$I \ge 2\sigma(I)$]	R_1 = 0.0445, wR_2 = 0.1018
Final *R* indexes [all data]	R_1 = 0.0571, wR_2 = 0.1072
Largest diff. peak/hole / e Å^{-3}	0.38/−0.37

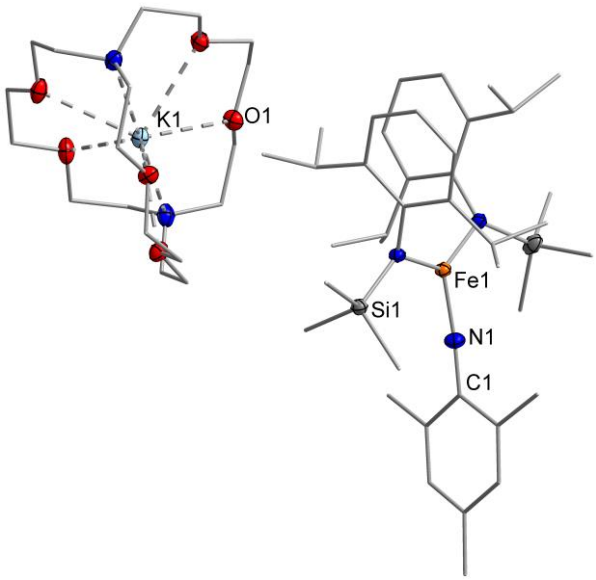

Figure S49. Molecular structure of K{crypt.222}[**1**] within the crystal.

Table S15. Crystal data and structure refinement for K{crypt.222}[**2**].

Identification code	K_crypt_2
Empirical formula	$C_{58}H_{99}FeKN_5O_6S_2Si_2$
Formula weight / g mol^{-1}	1177.67
Temperature / K	100.00
Crystal system	monoclinic
Space group	$P2_1/c$
a / Å	13.8538(8)
b / Å	24.6616(14)
c / Å	23.5229(13)
α / °	90
β / °	90.755(2)
γ / °	90
V / Å^3	8036.1(8)
Z	4
ρ_{calc} / g cm^{-3}	0.973
μ / mm^{-1}	0.361
F(000)	2540.0
Crystal size / mm^3	0.487 × 0.152 × 0.117
Radiation	MoKα (λ = 0.71073)
2Θ range for data collection / °	3.808 to 50
Index ranges	$-16 \le h \le 16$, $-29 \le k \le 29$, $-27 \le l \le 27$
Reflections collected	237874
Independent reflections	14145 [R_{int} = 0.1409, R_{sigma} = 0.0502]
Data/restraints/parameters	14145/0/693
Goodness-of-fit on F^2	1.048
Final *R* indexes [$I \ge 2\sigma(I)$]	R_1 = 0.0566, wR_2 = 0.1235
Final *R* indexes [all data]	R_1 = 0.0780, wR_2 = 0.1300
Largest diff. peak/hole / e Å^{-3}	0.38/−0.34

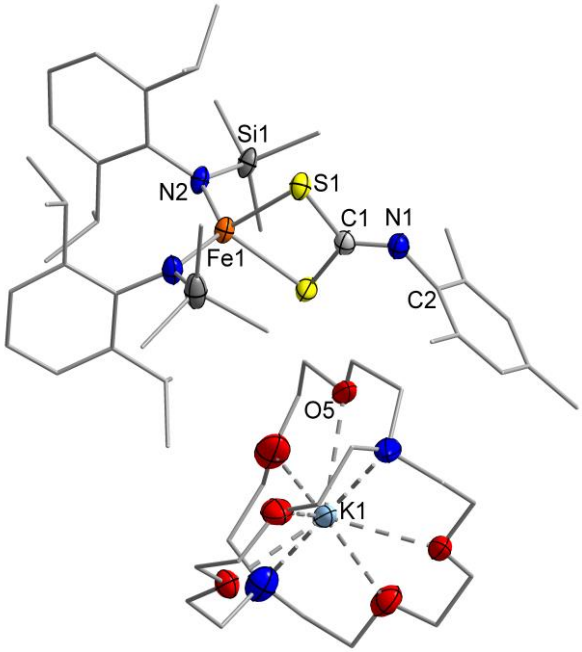

Figure S50. Molecular structure of K{crypt.222}[**2**] within the crystal.

References

[1] a) D. F. Evans *J. Chem. Soc.* **1959**, 2003; b) E. M. Schubert, *J. Chem. Educ.* **1992**, *69*, 62.

[2] J. M. Zadrozny, M. Atanasov, A. M. Bryan, C.-Y. Lin, B. D. Rekken, P. P. Power, F. Neese, J. R. Long, *Chem. Sci*. **2013**, *4*, 125.

[3] L. P. Spencer, R. Altwer, P. Wei, L. Gelmini, J. Gauld, D. W. Stephan, *Organometallics* **2003**, *19*, 3841.

[4] N. A. Giffin, M. Makramalla, A. D. Hendsbee, K. N. Robertson, C. Sherren, C. C. Pye, J. D. Masuda, J. A. C. Clyburne, *Org. Biomol. Chem.* **2011**, *9*, 3672.

[5] C. A. Laskowski, G. L. Hillhouse, *Organometallics* **2009**, *28*, 6114.

[6] S. Stoll, A. Schweiger, *J. Magn. Reson.* **2006**, *1*, 42.

[7] a) F. Neese, *Wiley Interdiscip. Rev.: Comput. Mol. Sci.* **2018**, *8*, e1327; b) F. Neese, *Wiley Interdiscip. Rev.: Comput. Mol. Sci.* **2012**, *2*, 73-78; c) F. Neese, F. Wennmohs, U. Becker, C. Riplinger, *J. Chem. Phys.* **2020**, *152*, 224108.

[8] a) W. Mao, F. W. Heinemann, A. Scheurer, D. Munz, K. Meyer, *Angew. Chem. Int. Ed.* **2021**, *60*, 16480-16486; b) A. Grünwald, S. S. Anjana, D. Munz, *Eur. J. Inorg. Chem.* **2021**, 4147 – 4166; c) S. Aghazada, M. Miehlich, J. Messelberger, F. W. Heinemann, D. Munz, K. Meyer, *Angew. Chem. Int. Ed.* **2019**, *58*, 18547-18551; d) G. Sieg, Q. Pessemesse, S. Reith, S. Yelin, C. Limberg, D. Munz, C. G. Werncke, *Chem. Eur. J.* **2021**, *27*, 16760-16767; e) S. Aghazada, D. Munz, F. W. Heinemann, A. Scheurer, K. Meyer, *J. Am. Chem. Soc.* **2021**, *143*, 17219-17225; f) S. Aghazada, D. Fehn, F. W. Heinemann, D. Munz, K. Meyer, *Angew. Chem. Int. Ed.* **2021**, *60*, 11138-11142.

[9] J. P. Perdew, M. Ernzerhof, K. Burke, *J. Chem. Phys.* **1996**, *105*, 9982-9985.

[10] C. Adamo, V. Barone, *J. Chem. Phys.* **1999**, *110*, 6158-6170.

[11] a) J. Tao, J. P. Perdew, V. N. Staroverov, G. E. Scuseria, *Phys. Rev. Lett.* **2003**, *91*, 146401; b) V. N. Staroverov, G. E. Scuseria, J. Tao, J. P. Perdew, *J. Chem. Phys.* **2003**, *119*, 12129-12137.

[12] C. van Wüllen, *J. Chem. Phys.* **1998**, *109*, 392-399.

[13] F. Weigend, R. Ahlrichs, *Phys. Chem. Chem. Phys.* **2005**, *7*, 3297-3305.

[14] E. Caldeweyher, S. Ehlert, A. Hansen, H. Neugebauer, S. Spicher, C. Bannwarth, S. Grimme, *J. Chem. Phys.* **2019**, *150*, 154122.

[15] F. Weigend, *Phys. Chem. Chem. Phys.* **2006**, *8*, 1057-1065.

[16] R. Bjornsson, F. Neese, S. DeBeer, *Inorg*. *Chem*. **2017**, *56*, 1470.

[17] B. O. Roos, P. R. Taylor, P. E. M. Siegbahn, *Chem. Phys.* **1980**, *48*, 157-173.

[18] G. Knizia, *J. Chem. Theory Comput.* **2013**, *9*, 4834-4843.

[xix] G. M. Sheldrick, *Acta Cryst*. **2015**, *71*, 3.

[xx] L. Farrugia, *J*. *Appl*. *Crystallogr*. **1999**, 32, 837.

[xxi] P. W. Betteridge, J. R. Carruthers, R. I. Cooper, K. Prout, D. J. Watkin, *J*. *Appl*. *Cryst*. **2003**, 36, 1487.

[xxii] *International Tables for X-ray crystallography* (Kynoch Press, Birmingham, England, 1974) *Vol*. *IV*.

[xxiii] *SADABS-2016/2* (Bruker, **2016**).